

Single electron transfer measurements through low temperature atomic force microscopy

Logan Fairgrieve-Park

Department of Physics

McGill University

Montreal, Quebec, Canada

August 2022

A thesis submitted to McGill University in partial fulfillment of the
requirements of the degree of Master of Science

© Logan Fairgrieve-Park, 2022

Abstract

Understanding the nature of electron transfer (ET) in quantum dots and single molecules can provide insight into both fundamental physical processes and the development of novel electronic and chemical systems. Traditional ET measurement techniques are not ideal as they either require a fixed probe or can only take an average measurement over a large area, obscuring the variety among individual structures. Single-electron electrostatic force microscopy (*e*-EFM) is an atomic force microscopy (AFM) technique that utilizes a movable, nanoscale probe to both induce charge transfer and measure transport properties. In this thesis, I provide an overview of the relevant of AFM theory and electron transport theory, including Coloumb and Franck-Condon blockade. I discuss the low temperature atomic force microscope (LT-AFM) used to quantify electron tunneling processes and outline measurements related to the noise and sensitivity of the system. Topographical AFM and *e*-EFM measurements of two different samples are presented: one consisting of self assembled quantum dots and the other a mixed ferrocene capped alkanethiol self assembled monolayer. This work has better defined the capabilities and performance of the LT-AFM and provides a framework for future measurements on ET pathways in single metalloenzymes.

Résumé

Comprendre la nature du transfert d'électrons dans les points quantiques et les molécules simples peut donner un aperçu des processus physiques fondamentaux ainsi que du développement de nouveaux systèmes électroniques et chimiques. Les techniques traditionnelles de mesure du transfert d'électrons ne sont pas idéales, car soit elles nécessitent une sonde fixe, soit elles peuvent seulement prendre une mesure moyenne sur une superficie large, ce qui obscurcit la variété entre les structures individuelles. La microscopie mono électronique à force électrostatique (e-MFE) est une technique de microscopie à force atomique (MFA) qui utilise une sonde nanométrique mobile afin d'inciter le transfert de charge et de mesurer les propriétés de transport. Dans cette thèse, je donne un aperçu détaillé de la théorie de la MFA et du transfert d'électrons, incluant le blocage de Coulomb et de Franck-Condon. Je discute du microscope à force atomique à basse température (MFA-BT), qui est utilisé pour quantifier les processus de l'effet tunnel monoélectronique, et je souligne les mesures reliées au bruit et à la sensibilité du système. Les mesures topographiques de la MFA et de l'e-EFM de deux échantillons différents sont également présentées. Le premier échantillon consiste de points quantiques autoassemblés et le deuxième est constitué d'une monocouche auto-assemblée d'alcanethiols recouverte de molécules de ferrocène. Ce travail a pu mieux définir la performance et la capacité du MFA-BT et a pu fournir un cadre pour des mesures futures sur le parcours du transfert d'électrons dans les métalloenzymes simples.

Acknowledgements

I would like to thank my supervisor, Peter Grütter, for giving me the opportunity to pursue this work. The LT-AFM is a challenging instrument and learning to use it has made me a better researcher. Your guidance, support, and encouragement of sharing within the group was always appreciated. I am incredibly grateful to José Bustamante, the resident LT-AFM expert, whose teaching and support was invaluable in learning how to use the system. I could not have asked for a better, more supportive partner to work and share the LT-AFM with. Thank you to my fellow MSc students in the group, Josephine Spiegelberg, Zixiao Zhang and Catherine Boisvert for the camaraderie and the enjoyable get togethers outside the lab. Many thanks to John Smeros for his assistance in the difficult task of procuring cryogenics and Robert Gagnon for his expertise on sample preparation and materials. I owe an additional thanks to entire Grütter group for the for the welcoming and productive environment they all created. Finally, thank you Michelle, Bev, and Alex for all your love and support over the last two years.

Contribution of Authors

The majority of the charge transfer theory presented in Chapter 2 has been adapted from the work of previous students performing *e*-EFM, specifically Romain Stomp, Antoine Roy-Gobeil and Lynda Cockins. The LT-AFM system described in Chapter 3 was originally developed as part of the PhD thesis of Mark Roseman. Subsequent generations of students have contributed improvements to the current design. The procedure for calculating LT-AFM sensitivity in section 3.1.1 was adapted from a Python script written by Harrisonn Griffin. AFM data shown in Figure 4.5 was taken by Catherine Boisvert. All other AFM data was taken by the Author

Table of Contents

Abstract	i
Résumé	ii
Acknowledgements	iii
Contribution of Authors	iv
List of Figures	x
1 Introduction	1
2 Theory	5
2.1 AFM Background	5
2.1.1 Static AFM	5
2.1.2 Dynamic AFM	6
2.1.3 Amplitude modulated AFM	8
2.1.4 Frequency modulated AFM	10
2.2 Charge Transfer Theory	12
2.2.1 Coloumb Blockade	12
2.2.2 Tunneling Rate Spectroscopy	14
2.2.3 Franck-Condon Blockade	16
3 Low Temperature AFM	18
3.1 Hardware	19
3.1.1 Microscope Body	20
3.1.2 Electronics	26
3.1.3 Vacuum and Cryogenics	27
3.2 Software and Control	30
3.3 Noise and Q Factor Determination	31

4	Sample Description and AFM Measurements	34
4.1	SAM and SAQD Samples	34
4.2	Topography Characterization	36
4.2.1	Time Dependent Changes in Monolayers	39
4.3	Charge Transfer Experiments Through <i>e</i> -EFM	40
4.3.1	Self Assembled Quantum Dot Measurements	42
4.3.2	Attempted Ferrocene SAM Measurements	44
4.3.3	Excitation Gain Complications and Unintended Self Oscillation	47
5	Conclusions and Outlook	49

List of Figures

1.1	Diagram of general AFM set up using interferometric detection of the cantilever	3
2.1	Typical force distance curve for cantilever tip interaction derived from the Lennard-Jones potential. The three highlighted areas show the general regions where contact mode, tapping mode and non-contact mode is operated	6
2.2	Normalized phase and amplitude of a generic harmonic oscillator described by Equations 2.3 and 2.4 with $\omega_0 = 50,000$ Hz and $Q = 400$	8
2.3	Reduction of cantilever oscillation amplitude that result either from a change in resonance frequency (Δf) or a change in effective Q factor (ΔQ)	9
2.4	(a) Schematic of AFM tip and QD system with a 2 dimensional electron gas (2DEG) as a conducting back substrate and InP as an insulating tunneling barrier. (b) Corresponding circuit diagram (adapted from	13
2.5	Normalized total tunneling rate as a function of electrochemical detuning $\Delta E(\alpha V_B)$ for a single degenerate level (black dashed), 2-fold degenerate level with shell filling of 0 and 1 (red and green), and a 4-fold degenerate level with a shell filling of 0 (orange) (adapted from	15
3.1	The LT-AFM and all of it's constituent parts. In this state it is currently removed from the dewar, which is necessary for performing repairs or changing samples. Interfacing between the microscope and the electronics is achieved through a series of feed-through tubes so only the force probe, sample and scanner need to be cooled down.	19

3.2	(a) Diagram of the LT-AFM body. (b) Image of the LT-AFM in it's open, assembled state. (c) Image of the LT-AFM with the can affixed, ready to be inserted into the dewar.	20
3.3	Cantilever mounted in place (a) using conductive epoxy and (b) clamped with a leafspring system. In (a) a piezo drive circuit is attached to the holder - a different holder was used in these experiments as an optical drive technique was used.	21
3.4	(a) Vertical view of the cantilever aligned with the fiber directly beneath. (b) Simultaneous side view of the cantilever with the fiber approached close to validate the alignment.	23
3.5	Image of the cantilever with the fiber positioned directly above it. The reflection of the the cantilever can be seen in the SAM on gold substrate sample and is used as a reference for approaching the sample and cantilever.	24
3.6	Detection laser signal and interferometer sensitivity as a function of fiber position with respect to cantilever (measured in both walker steps and nm). The nm position scale is derived from taking the separation of constructive interference peaks to be half of the laser wavelength ($\lambda/2=775$ nm). Sensitivity is the spatial gradient of the detection signal.	25
3.7	(a) Transfer of liquid helium and (b) liquid nitrogen. Because the liquid nitrogen dewar is pressurized, nitrogen will flow out when the valve is opened. The helium dewar is not pressurized, requiring manual pressurization with helium gas for transfer.	29
3.8	Fitted spectral density of the AFM cantilever non-driven resonance peak at 4 K using Equation 3.1. $\Delta f = \Delta\omega/2\pi = 161,619$ Hz, $Q = 113,802$ and $N_{base} = 26$ fm/ $\sqrt{\text{Hz}}$ are calculated from the fit. The data was taken using the FFT mode of MFLI lock-in amplifier and converted from photodetector voltage to femtometers using the calibration process shown in Figure 3.6. .	31

3.9	Fitted cantilever ring down and phase frequency response at 4 K using eqs. 3.2 and 2.4. The Q factor of the cantilever was found using both methods to be $\sim 140,000$	32
4.1	Cartoon diagram showing of the general structure of the two samples (a) Self assembled quantum dots and (b) mixed ferrocene capped and non-functionalized alkanethiol self assembled monolayer on gold	36
4.2	Topography images of a SAQD sample. (a) is a FM-AFM $3.3 \times 3.3 \mu\text{m}$ image captured using the LT-AFM at 4 K in non-contact mode. A frequency shift set-point of -15 Hz and a sample bias of -2 V was used. (b) is a FM-AFM 500×500 nm image captured using the LT-AFM at 77 K in non-contact mode. A frequency shift set-point of -20 Hz and a sample bias of 0 V was used. QDs appear as white blobs in the image.	37
4.3	Topography images of a ferrocene SAM on gold substrate. (a) is a FM-AFM $1 \times 1 \mu\text{m}$ image captured using the LT-AFM at 77 K in non-contact mode. A frequency shift set-point of -15 Hz and a sample bias of -0.1 V was used. (b) is a AM-AFM $1 \times 1 \mu\text{m}$ image captured using a Multimode Nanoscope III AFM in tapping mode. Ferrocene capped thiols appear as raised bumps both images. Grains of the template stripped gold also be discerned, though not very clearly because of the SAM covering the surface.	38
4.4	Topography images of a ferrocene SAM on gold sample captured using a Multimode Nanoscope III AFM in tapping mode. (a) is a $1 \times 1 \mu\text{m}$ image taken 6 days after removal of the sample from incubation solution and (b) is a $5 \times 5 \mu\text{m}$ image taken 35 days after removal of the sample from incubation solution. A longer sitting time post incubation results in a lower density but greater size of blobs on the sample surface.	40

4.5 Dissipation and frequency shift images of a QD site taken in constant height mode using the LT-AFM at 4 K with different bias voltages. (a) shows the frequency shift channel, while (b), (c) and (d) show dissipation channel. There are 5 observable QDs / CTs, with the topmost 3 being more visible in the dissipation images, while the bottom two are more visible in the frequency shift image. 42

4.6 (a) Frequency shift images of a SAM sample taken in FM-AFM mode using the LT-AFM at 4 K with a bias of 1V. CTs/ring sites are numbered 1 - 5. (b) shows voltage spectroscopy of CT 4 at a constant height. From top to bottom they are frequency shift, where the tunneling peaks are overshadowed by the electrostatic background; frequency shift with the electrostatic background removed; and the excitation gain for the cantilever drive. This excitation gain is analogous to dissipation (Equation 2.8). 44

4.7 Voltage excitation gain spectroscopy of CTs shown in Figure 4.6a. (a) Comparison of spectra captured with the tip centered over 3 different CTs. (b) Comparison of spectra of CT 5 with the tip directly over top, moved 5 nm off center and moved 10 nm off center. In each case, peak height and position is variable 46

1. Introduction

The phenomena underlying all chemical and electronic processes is the transfer and confinement of charge. The baking soda and vinegar volcano we all made by children can be understood as a sea of electrons rearranging and dragging their nuclei in tow, liberating hydrogen gas and sucking energy from the surroundings. The same movement of charges and transfer of energy occur in the technology we are increasingly turning to to power our world: photovoltaics and electrochemical energy storage.

Similarly, the function of modern digital computers relies on billions of near simultaneous controlled charge transfer events. As electronic chips and circuits are made smaller, greater precision is required in both their fabrication and operation. In quantum computing, this miniaturization is not only a desirable for space and power constraints, but necessary to the underlying function. Implementations of qubits that rely on quantized charge or electron spin require the precise confinement, control, and sensing of single electrons within quantum dots (QDs).

Given the minute scale of charge transfer in these chemical and electronic processes, it is often necessary to study them in temporally or spatially averaged ways. For example, cyclic voltammetry is a commonly used technique for characterizing the charge transfer processes of some chemical species [1]. Voltage and current measurements are made across a macroscopic sample, so information about any one specific molecule involved in the reaction cannot be obtained. This is despite the fact that the local environment around each molecule can be highly variable, making it's electrochemical behaviour different to and dependent on that of it's neighbors.

The ability to probe charge transfer at the nanoscale can provide more complete information of the state of a given molecule or QD. The classic implementation of this nanoscale probe is the single electron transistor (SET). An SET is a device that can con-

trol and detect single electron charging using coupled source, drain and gate electrodes, typically through a QD [2]. The common technique for producing these and other nanoelectronic devices involve precise nanolithography, fixing the target sensor on a surface [3,4].

However, not all charge transfer systems are compatible with SETs; for example, self assembled structures. Self assembly is a nano-fabrication technique that relies on stochastic processes to form structures of interest. It is often used to form organic structures, like DNA [5] and thiolate monolayers [6], and non organic structures, like QDs grown through metal organic vapor-phase epitaxy [7]. An effective way to study these surfaces on a molecule by molecule or QD by QD basis is using a movable gate/probe.

One implementation of a moveable gate/probe is the atomic force microscope (AFM). AFM was first demonstrated in 1986 by Binnig, Quate and Geber [8]. As a method of scanning probe microscopy, it consists of a flexible cantilever with sharp tip that can be accurately positioned on a surface. Tip sample forces are detected by deflection of the cantilever and a feedback loop is used to maintain tip sample separation. This is possible because there is typically a well defined relationship between tip sample interaction forces and tip sample separation distance. In the case of charge sensing, change in a molecule or QD will alter the force environment at the tip, which is then detected. Simultaneously, the capacitive influence of the tip at the site can induce charge transfer and change its state. A diagram of a basic AFM set up is shown in Figure 1.1.

Passive observation of single charging events was first described by Schönenberger and Alvarado [9]. The first description of an AFM technique for perturbing a charge site and observing single charging (single electron electrostatic force microscopy or *e*-EFM) by both 2D image and spectroscopy was given by Woodside on a nanotube QD [10]. This technique was then extended to *e*-EFM of self assembled quantum dots (SAQDs) [11], ground and excited state QD spectroscopy [12,13], and most recently tunneling rate spectroscopy of single charging events in QDs [14] and single redox molecules [15].

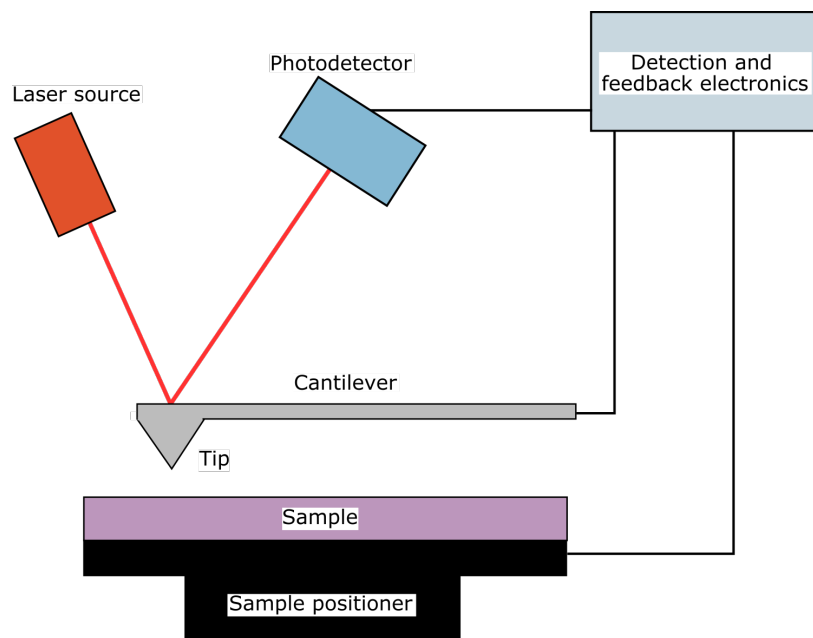


Figure 1.1: Diagram of general AFM set up using interferometric detection of the cantilever

The general intent of the research presented in this thesis is to continue and extend the work of Antoine Roy-Gobeil on *e*-EFM tunneling rate spectroscopy of single redox molecules; more specifically, ferrocene-terminated alkanethiols. These are ideal for AFM experimentation as they form an insulating self-assembled monolayer (SAM) on a gold electrode, allowing for electron transfer between the electrode and the ferrocene molecule at the end of the thiol. The MSc research of Harrisonn Griffin explored techniques for controlling and measuring the density and distribution of ferrocene molecules by including non-functionalized alkanethiols in the SAM [16]. That work was completed with the goal of producing SAMs with a wide range of local ferrocene densities to analyze the impact of neighboring ferrocenes on charging energies. Research completed for this thesis involves topographical measurements of ferrocene SAMs and low temperature *e*-EFM measurements of ferrocene SAMs and SAQDs. Additionally, the operation, maintenance, and characterization of the home built low temperature AFM (LT-AFM) used for *e*-EFM experiments is discussed.

The structure of this thesis is as follows. In Chapter 2 I describe the theory underlying different modes of AFM and charge transfer. In Chapter 3 I describe the design and operation of a custom made low temperature AFM used for e -EFM experiments. Additionally I discuss methods of cantilever Q factor and noise determination of the low temperature AFM, both relevant to achieving high performance e -EFM. In Chapter 4 I present room temperature, topographical and low temperature charge transfer measurements of SAMs and SAQDs. Chapter 5 is a summary and outlook for future single charging experiments.

2. Theory

2.1 AFM Background

2.1.1 Static AFM

To understand the dynamics of an atomic force microscopy, we can take the simplified view of the cantilever as a mass spring system acting as a simple harmonic oscillator. Here, the relationship between force on the cantilever tip, F , and the displacement of the cantilever tip from its equilibrium position, z , will be given by Hooke's law

$$F = -kz \tag{2.1}$$

where k is cantilever spring constant. Though F can be any force acting on the cantilever, we are typically interested in forces arising from interaction between the cantilever tip and the sample surface it is probing. A good starting point to describe a typical tip sample interaction is the Lennard-Jones (LJ) potential. Here, there is a repulsive tip sample regime that dominates at close distances due to Pauli exclusion and an attractive regime at farther distances arising from London dispersion forces. The force distance relationship described by the LJ potential is shown in Figure 2.1

There are different methods of AFM, but the earliest implementation is a form of static AFM known as contact AFM [8]. In this mode, the cantilever tip is brought into contact with the sample surface (repulsive regime). As the cantilever is moved over a surface, a feedback loop is used to measure the cantilever deflection and keep it constant by adjusting the z position. Assuming the cantilever deflection is only the result of sample topography, the change in z position can be read as the surface topography. This technique, though simple to implement, has a number of drawbacks. The tip or sample surface can

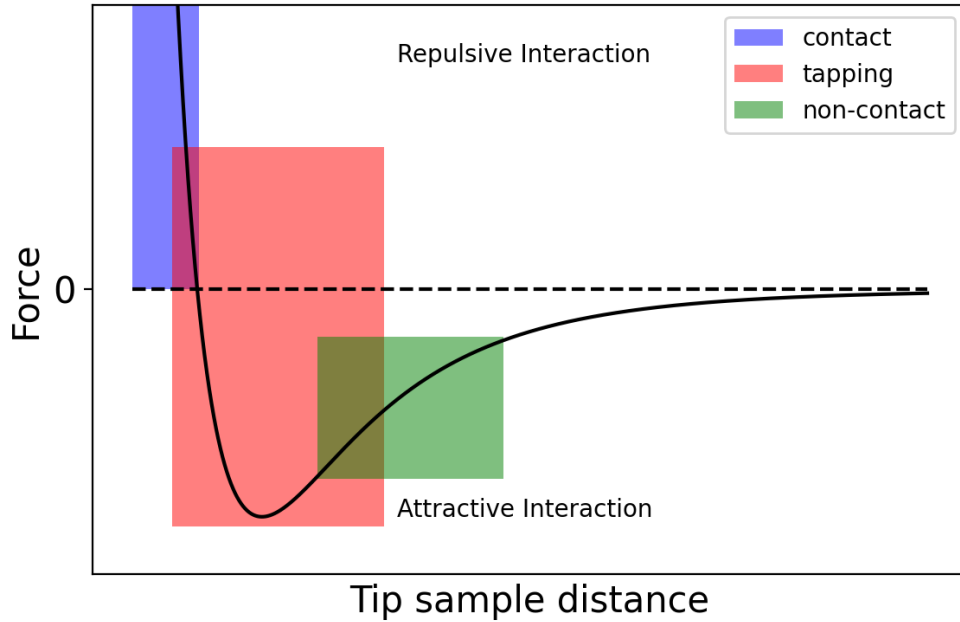


Figure 2.1: Typical force distance curve for cantilever tip interaction derived from the Lennard-Jones potential. The three highlighted areas show the general regions where contact mode, tapping mode and non-contact mode is operated

be altered or damaged as a result of sustained contact and motion of the tip on the sample. Additionally, in static AFM the cantilever deflection signal is essentially DC thus making it highly susceptible to $1/f$ noise.

2.1.2 Dynamic AFM

Although contact mode is a more straightforward implementation of AFM, dynamic AFM can offer noise advantages and can provide more information. In dynamic AFM, the cantilever is driven so that it oscillates at its resonance frequency. It is then the change in the cantilever's oscillation that provides the force/topography information. To understand this, we begin with a description of cantilever oscillation following the equation of motion of a damped, driven harmonic oscillator:

$$F_{applied} + F_{ts} + F_{noise} = m\ddot{z} + \gamma\dot{z} + kz \quad (2.2)$$

where $F_{applied}$ is an externally applied force acting on the cantilever, F_{ts} are forces provided by the tip sample interaction, F_{noise} is a mechanical/thermal noise component, m is the mass, and γ is the internal damping of the cantilever. Two important constants arise from this equation that define the cantilever dynamics: $\omega_0 = 2\pi f_0 = \sqrt{k/m}$, which is the resonance frequency of the cantilever and $Q = \omega_0/\gamma$ (Q -factor), which offers a more intuitive description of damping. For any oscillator, $2\pi Q$ is the ratio of energy stored to energy dissipated per oscillation. These two constants define the most efficient frequency to drive the oscillator at and its bandwidth.

Assuming a sinusoidal driving force $F_{applied} = F_0 \cos(\omega t - \phi)$, and negligible F_{ts} and F_{noise} , equations

$$A(\omega) = \frac{F_0/m}{\sqrt{((\omega_0^2 - \omega)^2 + (\omega\omega_0/Q))^2}} \quad (2.3)$$

$$\tan \phi = \frac{-\omega_0\omega}{Q(\omega_0^2 - \omega^2)} \quad (2.4)$$

describe the amplitude of the oscillator and the driver-oscillator phase lag respectively. These are plotted in Figure 2.2

During typical operation, F_{drive} is constant and F_{noise} is necessarily small, meaning the change in dynamics will be determined by change in F_{ts} . For small amplitudes, which is the usual operational case, the tip sample force will be approximated by

$$F_{ts}(d+z) = F_{ts}(d) + \left. \frac{\partial F}{\partial z} \right|_{z=0} z \quad (2.5)$$

where d is the tip sample distance. The rightmost term varies linearly with distance, so it can be grouped with the z term in Equation 2.2, providing a new effective spring constant of $k' = k + \left. \frac{\partial F}{\partial z} \right|_{z=0}$. Using a Taylor approximation, we can calculate the shift in resonance

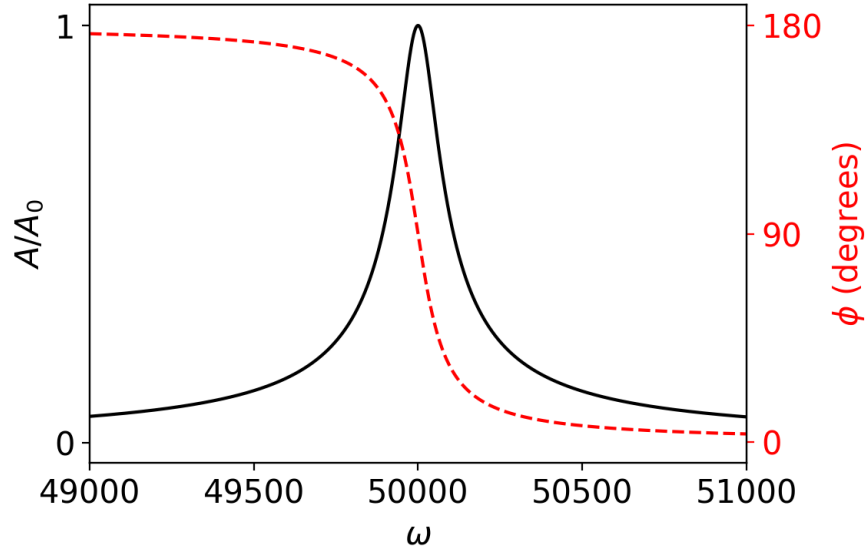


Figure 2.2: Normalized phase and amplitude of a generic harmonic oscillator described by Equations 2.3 and 2.4 with $\omega_0 = 50,000$ Hz and $Q = 400$

frequency resulting from this new effective spring constant to be:

$$\Delta\omega = -\frac{\omega_0}{2k} \left. \frac{\partial F}{\partial z} \right|_{z=0} \quad (2.6)$$

Though this exact derivation only applies in the small amplitude limit ($\partial F/\partial z \sim$ constant over oscillation amplitude), the end result for any oscillation amplitude is largely the same: a sample induced force gradient alters the cantilever dynamics, which can be measured. This change in cantilever dynamics is used provide an AFM feedback signal in one of two ways.

2.1.3 Amplitude modulated AFM

Amplitude modulated atomic force microscopy (AM-AFM) is a type of dynamic AFM where the feedback signal is the cantilever oscillation amplitude. First, the cantilever is driven at or near resonance with a constant driving amplitude as shown in Figure 2.3. As the tip sample interaction forces shift the resonance frequency, the cantilever will then

be driven "off" resonance, producing a lower oscillation amplitude. Using proportional-integral (PI) control, the cantilever can be made to approach a sample until an amplitude set point (corresponding to a specific frequency shift and thus tip sample interaction) is reached and maintain that set point. The z motion required to maintain the amplitude set point is recorded as the topography signal.

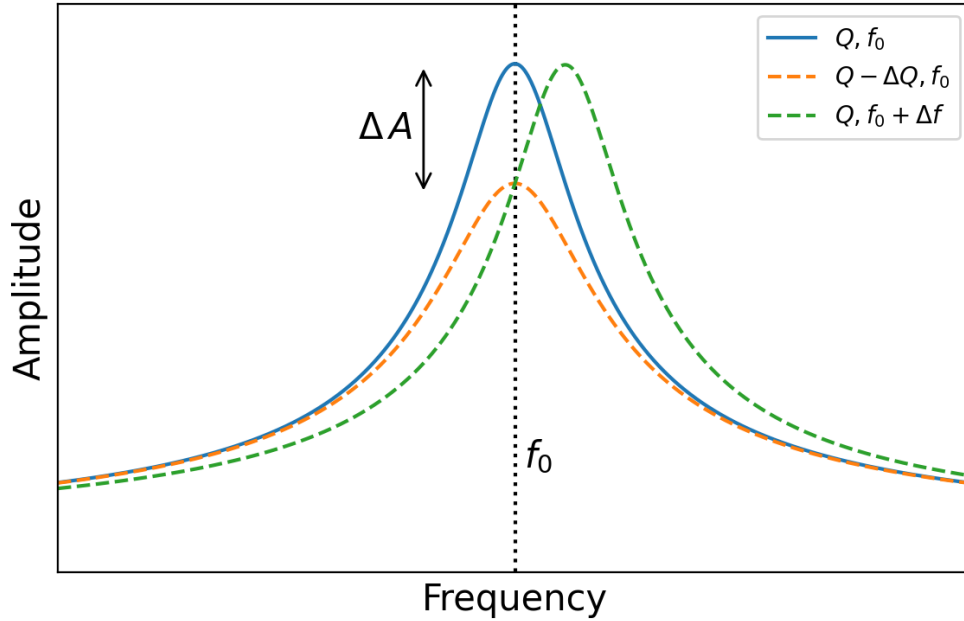


Figure 2.3: Reduction of cantilever oscillation amplitude that result either from a change in resonance frequency (Δf) or a change in effective Q factor (ΔQ)

For the amplitude of oscillation to decrease the cantilever must dissipate energy through friction with itself or surroundings. The cantilever will take Q oscillations to reduce by 50%, corresponding to a time of $\tau \approx Q/(f_0\pi) = 0.4$ ms for $Q = 100$ and $f_0 = 70,000$ Hz, typical values for a cantilever in air. This time constant is small enough to allow for relatively fast scanning speeds. A lower Q generally allows for faster data capture rate in AFM. However, a higher Q provides a higher signal to noise ratio (SNR) given the steeper amplitude/phase curve. As higher SNR is desirable, there is an inherent tradeoff in AM-AFM between fast scanning and high sensitivity. Operating at lower pressures drastically

increases cantilever Q due to reduced friction with air making AM-AFM too slow to use effectively in vacuum.

A related consideration is that a higher cantilever drive amplitude can produce a higher SNR but result in a breakdown of amplitude limit assumptions. To achieve reasonable amplitude reduction in the high amplitude limit, the cantilever will swing far away where the tip sample forces are low, to very close where repulsive contact forces dominate. This is known as "tapping" mode and the range of tip sample distance is shown in Figure 2.1. As the tip enters the repulsive regime, it can result in the changes in the sample surface as well as non-linear tip-sample interactions characteristic of short-range interactions.

One other consequence of using amplitude as a feedback signal is the difficulty of distinguishing between conservative and non conservative forces between the tip and sample. A conservative force, such as electrostatic, will cause the cantilever frequency to shift, reducing its amplitude. A non-conservative force, like tip sample friction, will decrease the effective Q factor of the cantilever, essentially "broadening" and reducing the amplitude curve. For applications where discerning conservative and non-conservative interactions is important (as discussed in section 2.2.2), AM-AFM is a poor choice.

Given that AM-AFM is easy to implement but carries certain drawbacks, it is a technique best suited and often used for generic topography characterization of samples in air.

2.1.4 Frequency modulated AFM

In frequency modulated atomic force microscopy (FM-AFM), the feedback signal is the frequency shift of the cantilever oscillation, which is directly monitored. Frequency response in FM-AFM is very fast, even at high Q (> 1000). Given that amplitude reduction isn't necessary in FM-AFM, it is often operated in a "non-contact" mode where the tip sample distance is maintained in the low force attractive regime shown in Figure 2.1.

One substantial difference in FM-AFM is that the cantilever is not driven at a fixed frequency, but is instead always driven at the resonance frequency, even as it varies due to tip sample interaction. This technique is called "self oscillation" [17] as the oscillation signal of the cantilever is phase shifted 90° and used as the driving signal. The frequency shift, as the feedback signal, is tracked using a phase-locked-loop and used to maintain tip sample separation through PI control.

The ability to distinguish conservative and non conservative interactions is a useful consequence of self oscillation. For a constant driving force at resonance, the change in amplitude associated with a change in resonance frequency due to a conservative interaction is minimal. However, the change in effective Q associated with non-conservative/dissipative interaction will cause a significant reduction in amplitude (Figure 2.3). For this reason, a second feedback loop can be used to measure dissipation, γ . The oscillation amplitude is set by applying a variable gain to the self oscillation/drive signal in conjunction with PI control. As the dissipation increases, the drive gain will increase to compensate and keep the amplitude the same.

The intrinsic energy loss per cycle of a cantilever is given by [18]

$$E_0(A) = \frac{\pi k A^2}{Q} \quad (2.7)$$

where A is the cantilever amplitude. The energy loss due separately to tip sample interaction is

$$E_{ts} = E_0 \left(1 - \frac{\gamma}{\gamma_0}\right) = E_0 \left[\frac{A_{exc}}{A_{exc,0}} - \frac{f}{f_0} \right] \approx E_0 \left[\frac{A_{exc} - A_{exc,0}}{A_{exc,0}} \right] \quad (2.8)$$

where A_{exc} is the drive/excitation gain required to maintain the set-point amplitude during tip sample interaction, $A_{exc,0}$ is the drive/excitation gain required to maintain the set-point amplitude during free oscillation/no tip sample interaction, and γ_0 is the intrinsic dissipation of the cantilever. During normal operation the change in energy due to frequency shift is negligible ($f/f_0 \approx 1$) yielding the approximate form on the right in Equation 2.8. Though A_{exc} is the value that is measured, γ in units of Hz is the value that

is typically reported and is found from Equation 2.8 to be

$$\gamma = \left[1 - \left(\frac{A_{exc} - A_{exc,0}}{A_{exc,0}} \right) \right] \gamma_0 = \left[1 - \left(\frac{A_{exc} - A_{exc,0}}{A_{exc,0}} \right) \right] \frac{\omega_0}{Q} \quad (2.9)$$

2.2 Charge Transfer Theory

2.2.1 Coloumb Blockade

Charge transfer is typically understood in the context of a current-voltage characteristic: the flow of charge in response to a potential difference. For most conductors this characteristic is Ohm's law, where current is linearly dependent on voltage and set by the resistance of the material. For more complex systems, such as diodes where Ohm's law does not hold, current can still be described as some continuous function of voltage. Despite the fundamental nature of charge quantization, a continuous model is adequate to describe most electronic systems as either zero or an incredibly large number of electrons will be transferred each second.

However, for the smallest electronic structures, quantum dots (QDs) and single molecules, a continuous model of charge is insufficient. For structures of this size, the displacement of one electron can drastically change the energy landscape, preventing the subsequent movement of charge. The basic premise underlying this quantized charge transfer is Coulomb Blockade, where the tunneling of an electron onto a QD will alter the electric field enough to prevent subsequent tunneling at that voltage. Figure 2.4 shows a model of how single charge transfers can be induced and Coulomb blockade observed using AFM. In this set up the cantilever is close enough to influence the QD, but far enough that tunneling will only occur between the QD and the back electrode. The free energy of the QD is given by the equation [20]

$$W = \frac{q^2}{2C_\Sigma} - \frac{C_{tip}}{C_\Sigma} qV_B = \frac{1}{2} \frac{C_{sub}C_{tip}}{C_\Sigma} V_B^2 \quad (2.10)$$

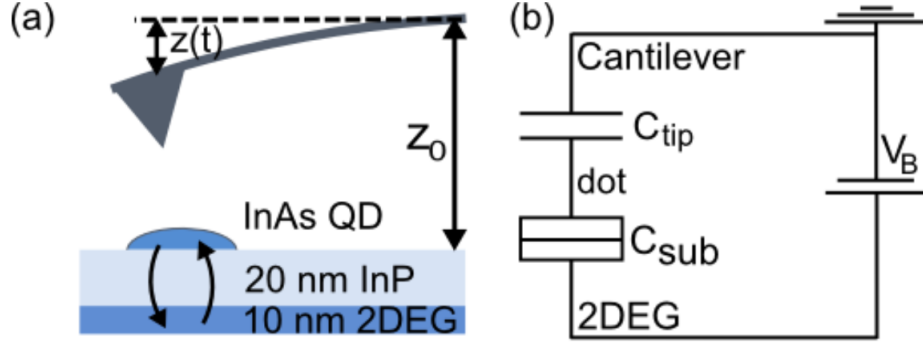


Figure 2.4: (a) Schematic of AFM tip and QD system with a 2 dimensional electron gas (2DEG) as a conducting back substrate and InP as an insulating tunneling barrier. (b) corresponding circuit diagram (adapted from [19]).

where q is the QD charge, V_B is the bias voltage between tip and substrate, C_{tip} is the capacitance between the tip and QD, C_{sub} is the capacitance between the QD and substrate, and $C_{\Sigma} = C_{sub} + C_{tip}$. An electron will tunnel onto or off of the dot if it is energetically favourable, that is, the free energy is reduced. Through minimization of the QD free energy, it's charge can be found to be [11]

$$q = -ne = -e \text{Int} \left(\frac{C_{tip}V_B}{e} + \frac{1}{2} \right). \quad (2.11)$$

Given this equation, the charge of the QD will only depend on the V_B and $C_{tip}(z)$. The resulting electrostatic force on the tip from charge q on the dot can be found by taking the gradient of Equation 2.10

$$F = \frac{\partial W}{\partial z} = \frac{1}{2} \frac{\partial C_{series}}{\partial z} \left(V_B - \frac{q}{C_{sub}} \right)^2 \quad (2.12)$$

where $C_{series} = C_{tip}C_{sub}/(C_{tip} + C_{sub})$. When operating in dynamic non-contact mode, the the tip sample capacitance will constantly be changing because of the oscillatory motion of the cantilever: $C_{tip}(z_0 + z(t))$. There will be certain values of V_B and $C_{tip}(z_0)$ where the change in capacitance due to cantilever motion is sufficient to change the charge state of the QD from $q = -ne$ to $q = -(n + 1)e$ over the period of oscillation.

As tunneling is a probabilistic process, an extra electron can be understood to tunnel onto and off of the dot at a given rate, Γ_+ and Γ_- respectively, when averaged over many oscillations. The periodic change in charge of the dot results in a periodic force on the cantilever that has in phase and out of phase components with the cantilever's motion. As outlined in sections 2.1.2 and 2.1.4, this will result in a cantilever frequency shift (Δf) and dissipation (γ) increase. By performing AFM spectroscopy (measuring response to change in V_B) or imaging (measuring response to change in C_{tip} resulting from change in tip sample spacing), the energy level structure within QDs can be probed through observation of the induced charge transfer. This technique of controlling and sensing single charging with AFM is known as single electron electrostatic force microscopy (*e*-EFM). An overview of this technique was provided in 2017 by Miyahara et al [21].

2.2.2 Tunneling Rate Spectroscopy

Though dissipation and frequency shift measurements can yield information on the energy level structure of QDs, they are purely a result of the underlying process: the periodic tunneling of electrons in and out of the structure. Usefully, in specific circumstances, the dissipation and frequency shift signal can be used to determine the exact electron tunneling rates.

The simplified master equation of the probability of finding 1 extra electrons on the QD is given by [12]

$$\partial_t \langle P \rangle = -\Gamma_- \langle P \rangle + \Gamma_+ (1 - \langle P \rangle) \quad (2.13)$$

Given the in phase and out of phase component of the tunneling electron, an in phase and out of phase force component will be applied on the cantilever, resulting in a frequency shift and dissipation shift of [14]

$$\Delta\omega = -\frac{\omega_0 A}{2\pi k_0 a} \int_0^{2\pi/\omega_0} dt \cos(\omega_0 t) \langle P(t) \rangle \quad (2.14)$$

$$\Delta\gamma = -\frac{\omega_0^2 A}{\pi k_0 a} \int_0^{2\pi/\omega_0} dt \sin(\omega_0 t) \langle P(t) \rangle \quad (2.15)$$

where a is the cantilever oscillation amplitude and $A = -(2E_c V_B/e)(1 - \alpha)\partial C_{tip}/\partial z$ is the dot-cantilever coupling strength with charging energy $E_c = e^2/2C_\Sigma$, and lever arm $\alpha(x, y, z) = C_{tip}/C_\Sigma$. Equation 2.14 and 2.15 can be simplified in the weak coupling regime ($aA \ll k_B T$) to

$$\Delta\omega = -\frac{\omega_0 A^2}{2k_0} \frac{\Gamma'_+ \Gamma'_\Sigma - \Gamma_+ \Gamma'_\Sigma}{\Gamma_\Sigma^2 + \omega^2} \quad (2.16)$$

$$\Delta\gamma = \frac{\omega_0^2 A}{k_0 \Gamma_\Sigma} \frac{\Gamma'_+ \Gamma'_\Sigma - \Gamma_+ \Gamma'_\Sigma}{\Gamma_\Sigma^2 + \omega^2} \quad (2.17)$$

Finally, the total tunneling rate can be described completely as a function of AFM measurable values

$$\Gamma_\Sigma = -2\omega_0 \frac{\Delta\omega}{\Delta\gamma} \quad (2.18)$$

The tunneling rate is highly dependent on characteristics of the QD system (degeneracy,

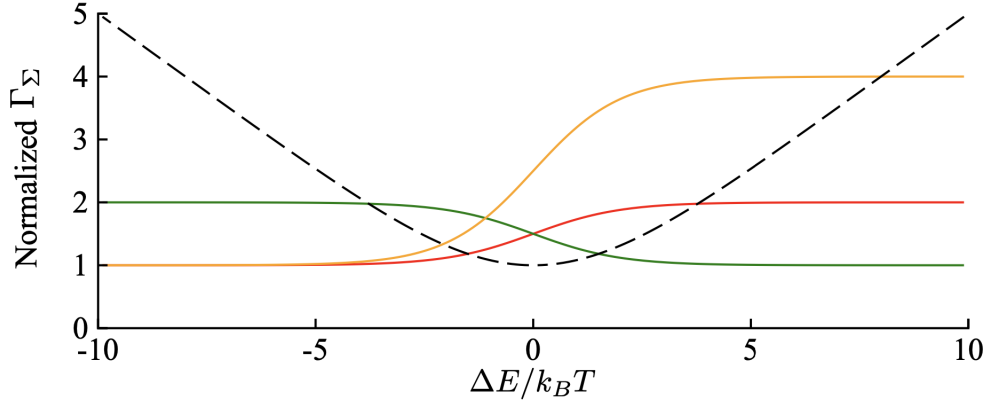


Figure 2.5: Normalized total tunneling rate as a function of electrochemical detuning $\Delta E(\alpha V_B)$ for a single degenerate level (black dashed), 2-fold degenerate level with shell filling of 0 and 1 (red and green), and a 4-fold degenerate level with a shell filling of 0 (orange). Adapted from [14].

density of states), as shown in simulated data in Figure 2.5. By comparing the tunneling rate to the predicted behaviour of a given QD, conclusions can be drawn about its energy level structure [14].

2.2.3 Franck-Condon Blockade

Single electron transport through molecules has been shown through experiment to closely follow the Coloumb blockade behaviour observed in QDs [22]. However, there are unique characteristics of molecules that result in differences in electron transport properties. Most QDs are physically realized as mesoscopic particles: blobs of material small enough to demonstrate measurable Coloumb blockade effects. However, as the particle size is decreased further to the single molecule level, a description of the charge transfer process must take into account electron-phonon interactions, which begin to dominate. These electron phonon interactions arise from nuclear reorganization, where there is a change in energy associated with the change in nuclear coordinates of the molecule [23]. This process occurs as electron changes the charge (redox) state of the molecule. This electron transport mediated by electron-phonon coupling in the molecular regime is known as Franck-Condon blockade, and is essentially Coulomb blockade in the strong electron-phonon coupling regime [24].

Understanding the energy associated with nuclear reorganization is relevant as it largely determines electron transfer behaviour and reactions in organic and electrochemical systems [25]. Unlike the QD/Coulomb blockade case where only the probability of residing in the n (ground) and $n + 1$ (excited) charge state has to be considered, the molecule/Franck-Condon blockade case requires that we consider the n (oxidized) and $n + 1$ (reduced) states and simultaneously the nuclear/vibronic states. Starting with just a single vibronic state, the electron transfer rate between the back-electrode, S , and the molecule, m , in the Franck-Condon regime can be described by the equation

$$k_{S \rightarrow m} = \frac{2\pi}{\hbar} |M|^2 |\langle \chi_0^+ | \chi_m \rangle|^2 \int D_S(\varepsilon) f(\varepsilon) \delta(\varepsilon - \varepsilon_m) d\varepsilon \quad (2.19)$$

where \hbar is Planck's constant, $|M|^2$ is the electronic coupling, χ is the vibronic state, ε is the single-particle energy, D_S is the back electrode density of states, and $f(\varepsilon)$ is the Fermi-

Dirac distribution. This model is sufficient in the low energy limit where the tip-sample bias and oscillation amplitude are only excite the lowest lying vibrational mode.

In the higher energy case, multiple vibronic states can be excited. Here, the forward k_f and backward k_b electron transfer rates are given by

$$k_f = \frac{2\pi}{\hbar} |M|^2 D_S \int f(\varepsilon) \sum_m \left[|\langle \chi_0^+ | \chi_m \rangle|^2 \delta(\varepsilon - \varepsilon_{mol} - m\hbar\omega) \right] d\varepsilon \quad (2.20)$$

$$k_b = \frac{2\pi}{\hbar} |M|^2 D_S \int [1 - f(\varepsilon)] \sum_n \left[|\langle \chi_0 | \chi_n^+ \rangle|^2 \delta(\varepsilon - \varepsilon_{mol} + n\hbar\omega) \right] d\varepsilon \quad (2.21)$$

where $\varepsilon_{mol} = E_{red} - E_{ox}$, the total energy difference between the reduced and oxidized states, and ω is the characteristic frequency of the vibrational mode.

The presence of one or more vibronic states result in the tunneling rate as a function of electrochemical detuning to be modulated by many apparent step like features, unlike the smooth form for Coloumb blockade seen in Figure 2.5. This modulation of tunneling rate will result in an altered time dependent charging of the molecule and subsequent electrostatic force, which will be reflected in the cantilever frequency shift Δf and dissipation γ . Observation of Franck-Condon blockade consistent with a single vibronic state model has previously been observed in ferrocene SAM experiments using the LT-AFM [15].

3. Low Temperature AFM

Except for uniquely designed samples [26], electron transfer effects like Coulomb and Franck-Condon blockade are only observable at low temperatures. The charging energy of the dot must be much greater than the thermal energy of the electrons ($E_c \gg k_B T$) or thermal electrons will tunnel over the energy barrier without perturbation. Experiments have shown these energy scales to be on the order of 31 meV for charge states in quantum dots [12] and 4.6 meV for vibronic states in molecules [14].

For this reason, we perform single electron charging experiments at low temperatures using a home built, low temperature atomic force microscope (LT-AFM), which is designed to be cryogenically cooled. Using liquid helium, a temperature of 4K can be reached with a very low associated thermal electron energy of $k_B T \approx 0.3$ meV. There are other advantages of AFM experimentation at low temperatures. A higher SNR can be achieved in experiments as thermal force noise of a cantilever is proportional to \sqrt{T} [27]. Creep on piezoelectric components is slowed at low temperatures, reducing sample and cantilever drift. Additionally, practice has shown that low temperatures result in higher cantilever Q factors, increasing force sensitivity.

There are certain disadvantages associated with operating an AFM at low temperatures. Repeated thermal cycling can result in stress and wear of microscope components, decreasing their lifetime and increasing failure rate. The LT-AFM also suffers from long turn-around time. Once the microscope has been cooled down, repairs and changes to the system can't be made until it is removed from the cryogenic environment and allowed to return to room temperature. Finally, long lead times associated with liquid helium supply and the sensitive nature of some samples can make the timing of experimentation challenging.

The original design and construction of the LT-AFM is described in the PhD thesis of Mark Roseman [28], though subsequent generations of students and researchers have contributed to the current design.

3.1 Hardware

The entire LT-AFM system consists of three main parts: the body of the microscope containing the force probe system and positioners, the electronics used for interfacing and controlling various components, and the dewar and vibration isolation system that the microscope is inserted into for low temperature measurements. The complete LT-AFM system is shown in Figure 3.1

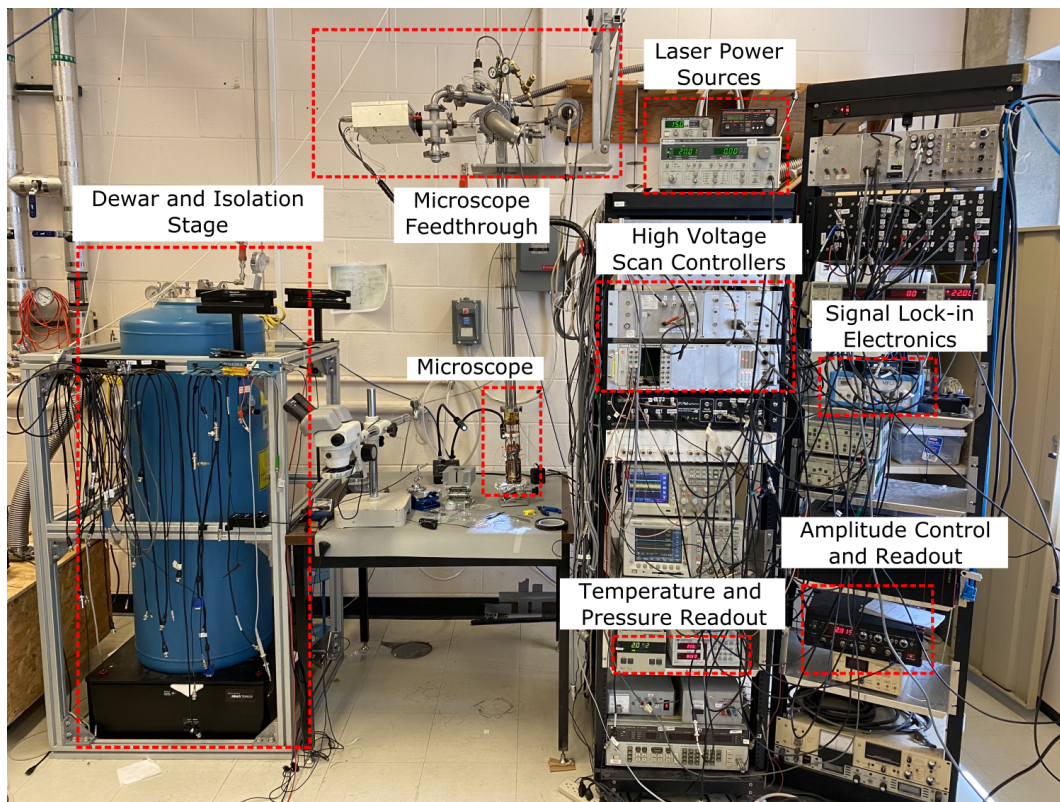


Figure 3.1: The LT-AFM and all of its constituent parts. In this state it is currently removed from the dewar, which is necessary for performing repairs or changing samples. Interfacing between the microscope and the electronics is achieved through a series of feed-through tubes so only the force probe, sample and scanner need to be cooled down.

3.1.1 Microscope Body

Due to the requirement of operating the LT-AFM at low temperatures, the microscope has been designed such that it can be inserted into a dewar that is then filled with liquid nitrogen or liquid helium for cooling. As a result, it is necessarily small and compact with larger electronics and larger components moved away from the microscope body but kept accessible via feed-through tubes. The microscope has an open design can be disassembled for sample changes and repairs. During experimentation, a can is placed around the body of the microscope and secured with eight screws before it is inserted into the dewar. As common o-ring materials do not stay elastic at low temperatures, indium is used to form a seal. A piece of 1mm indium wire is placed between the can and the feed-through system and by evenly tightening the screws it is compressed to seal the joint. The microscope body is pictured in Figure 3.2. As the LT-AFM is highly sensitive to external vibrational noise, the body is suspended by a long, spring like bellows. This serves to filter mechanical noise with frequencies lower than that of the bellows (~ 2 Hz).

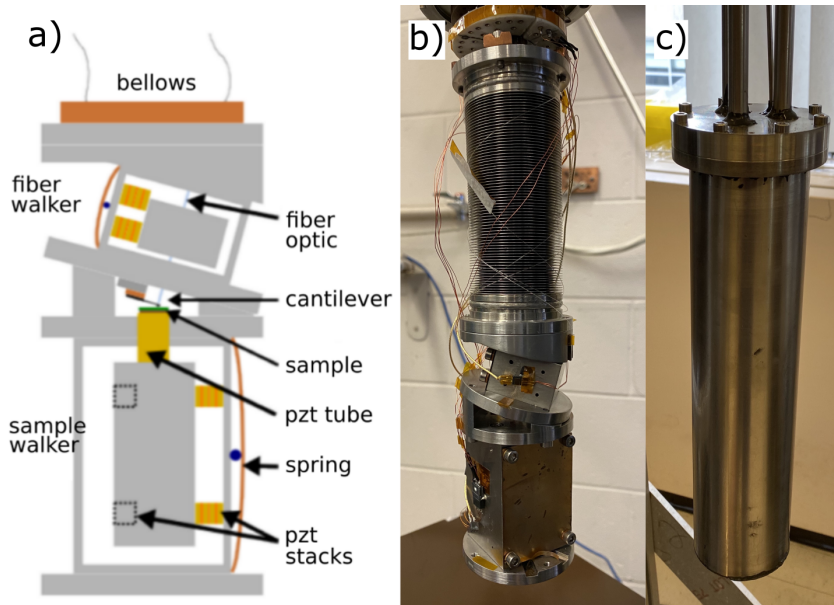


Figure 3.2: (a) Diagram of the LT-AFM body. (b) Image of the LT-AFM in its open, assembled state. (c) Image of the LT-AFM with the can affixed, ready to be inserted into the dewar.

Nanosensors 240AC-PP cantilevers are used for performing charging experiments with the LT-AFM [29]. They have a nominal spring constant of 20 N/m, resonance frequency of 70 kHz and are coated on all sides with platinum to ensure high reflectivity for optical sensing as well as high conductivity. The cantilevers are approximately 240 μm long and have a tip diameter of < 25 nm. A small tip size is important for high spatial resolution when imaging structures on the nanometer length scale, so care is taken to preserve tip sharpness. The cantilevers themselves are carved out of larger chips that are millimeters in size allowing them to be handled and affixed in the LT-AFM system more easily.

To secure the cantilever in place, the chips are affixed to a mounting block that interfaces the microscope body. This is done either using a conductive epoxy to glue the chip down or with the use of a leafspring system that clamps the chip to a silicon holder with a single point of contact. Both of these mounting methods are shown in Figure 3.3.

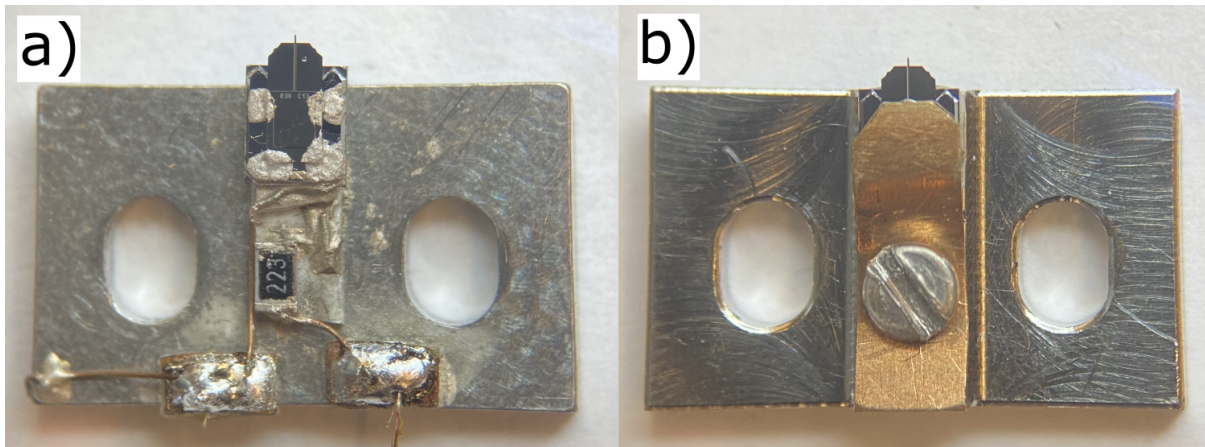


Figure 3.3: Cantilever mounted in place (a) using conductive epoxy and (b) clamped with a leafspring system. In (a) a piezo drive circuit is attached to the holder - a different holder was used in these experiments as an optical drive technique was used.

Achieving a good cantilever mounting is important as it will affect the intrinsic Q factor of the cantilever. If not affixed securely, there will be a large amount of energy loss through vibrations in the chip, making it difficult to drive the cantilever to a high enough amplitudes and impacting sensitivity. Practice had shown the epoxy method (Figure 3.3a)

to produce the most consistently high performance. Therefore, this epoxy method was used.

Cantilever motion is detected using an optical system that consists of 1550 nm laser diode, optical circulator and photodiode. The system is an interferometer, where light bouncing off of the cantilever interferes with itself, changing the intensity incident on the photodiode and allowing the relative cantilever position to be determined. To drive the cantilever an optical system is also used, which consists of a higher power, 1310 nm laser diode with a beam that is directed at the cantilever along the same path as the sensing laser. The DC output of the drive laser is modulated by an AC signal (in the case of self oscillation the optical detection signal) at the resonance frequency. The cantilever is driven as a result of oscillatory radiation pressure [30]. This optical drive system was a more recent addition to the LT-AFM, as it was found that an optical drive provided a cleaner cantilever oscillation with less phase noise [31]. Piezo-excitation was used in a prior implementation of the LT-AFM, which relies on a piezoelectric material to drive the cantilever by shaking the entire mounting block. This technique provides a high drive amplitude, but excites multiple spurious resonances in the system resulting in increased noise.

Both the detection and drive laser need to be directed so they are incident on a concentrated spot near the end of the cantilever. This is to provide both high drive efficiency and detection sensitivity. To accomplish this, a fiber optic system is used. By coupling both laser diodes to a single optical fibre, the work of aligning the optics is reduced. When aligning the fiber, the LT-AFM body is separated into two parts: the one containing the sample and the other containing the fiber and cantilever. During alignment, the position of the cantilever and fiber are visually monitored from both an overhead and side view. The fiber is approached towards the cantilever until it is nearly touching and the cantilever mounting block is adjusted until the cantilever tip is centered over the fiber. Once it has been aligned the mounting block screws are tightened, locking the alignment in

place. A well aligned cantilever is shown in Figure 3.4. Once aligned the two microscope halves can be rejoined and screwed back into place.

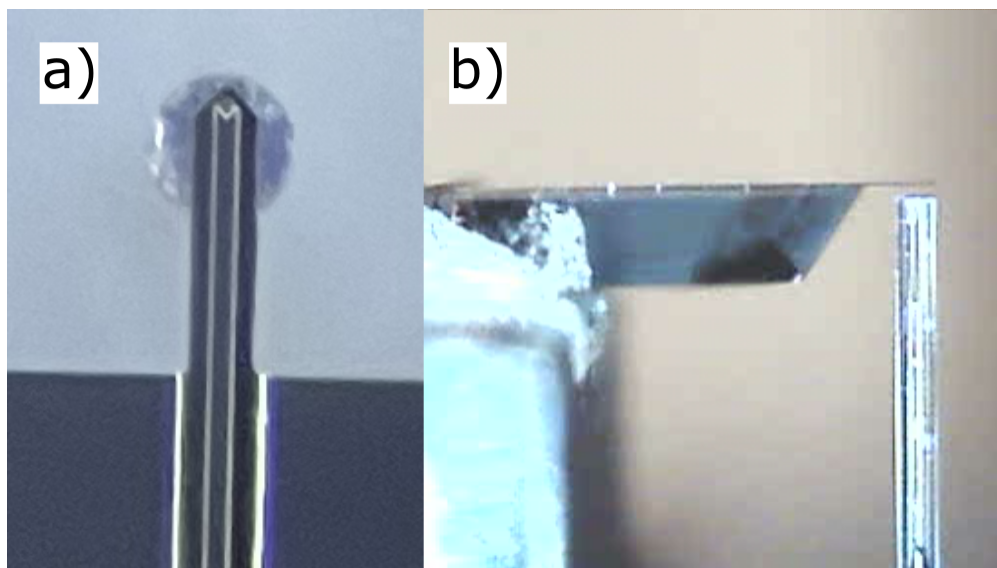


Figure 3.4: (a) Vertical view of the cantilever aligned with the fiber directly beneath. (b) Simultaneous side view of the cantilever with the fiber approached close to validate the alignment.

The function of the LT-AFM relies on parts that must be able to move both at room and cryogenic temperatures. These include the fiber, which must be aligned and approached close to the cantilever, and the sample, which must be able to move in range of the cantilever with relatively large steps and small, well defined steps during imaging and topographical positioning. Dynamic positioning of the microscope components is done with piezoelectric materials. Piezoelectric materials deform in a linear, predictable way under the presence of an electric field [32]. In practice, this is achieved by applying a voltage across the material, causing it to expand or contract.

A piezo tube is used for fine sample motion in 3-dimensions during imaging or topographical positioning. This common implementation of AFM sample positioning relies on a hollow tube of piezo material, with one electrode on the inside surface and four quadrant electrodes on the outside surface. By controlling the voltage on the five electrodes, the tube can be made to deform in any direction with fast response times and

minimal hysteresis. The sample rests on top of the tube, changing position in response to the tube deformation. However, the range of the deformation is small (~ 20 μm in x and y and < 1 μm in z), requiring that the sample be brought into close range of the tip before imaging or xy positioning.

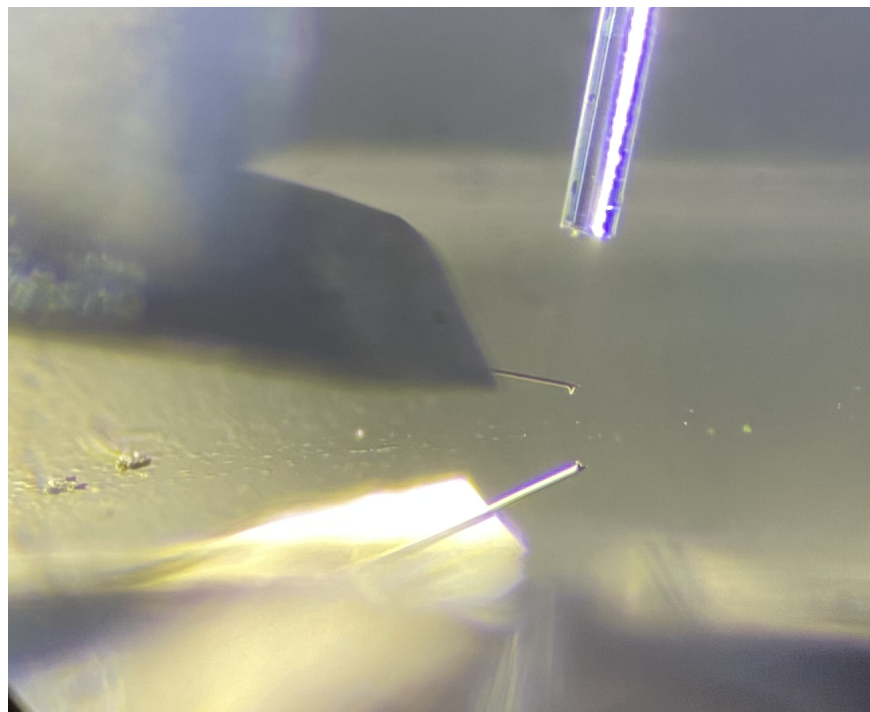


Figure 3.5: Image of the cantilever with the fiber positioned directly above it. The reflection of the the cantilever can be seen in the SAM on gold substrate sample and is used as a reference for approaching the sample and cantilever.

To produce the large steps required for positioning the optical fiber or approaching the sample from far distance to the tip, piezo “walkers” are used, which are able to move the components using slip stick motion. They consist of multiple square layers of piezoelectric material separated by insulating oxide layers. A sawtooth voltage signal is applied to entire stack which produces a large expansion followed by a fast contraction as the voltage drops to zero. This rapid deformation causes the stack to briefly overcome the friction holding it against the fiber or sample holder, making it “jump” to a new position. The position of the walkers within the LT-AFM is shown in Figure 3.2a. Using this method, the sample and fiber can be moved 10s of millimeters with sub micrometer steps.

After a sample is inserted in the LT-AFM, the fiber, cantilever and sample are all brought into relatively close contact to validate alignment and speed up the final sample approach after the can is closed and the microscope is inserted into the dewar. This alignment is shown in Figure 3.5. The spacing of the sample, microscope and cantilever will change as a function of temperature, requiring that they be reasonably separated before cooling. When closed, the sample is slowly approached until a tip sample force is detected by taking single sample walker steps while sweeping the entire z range of the piezo tube.

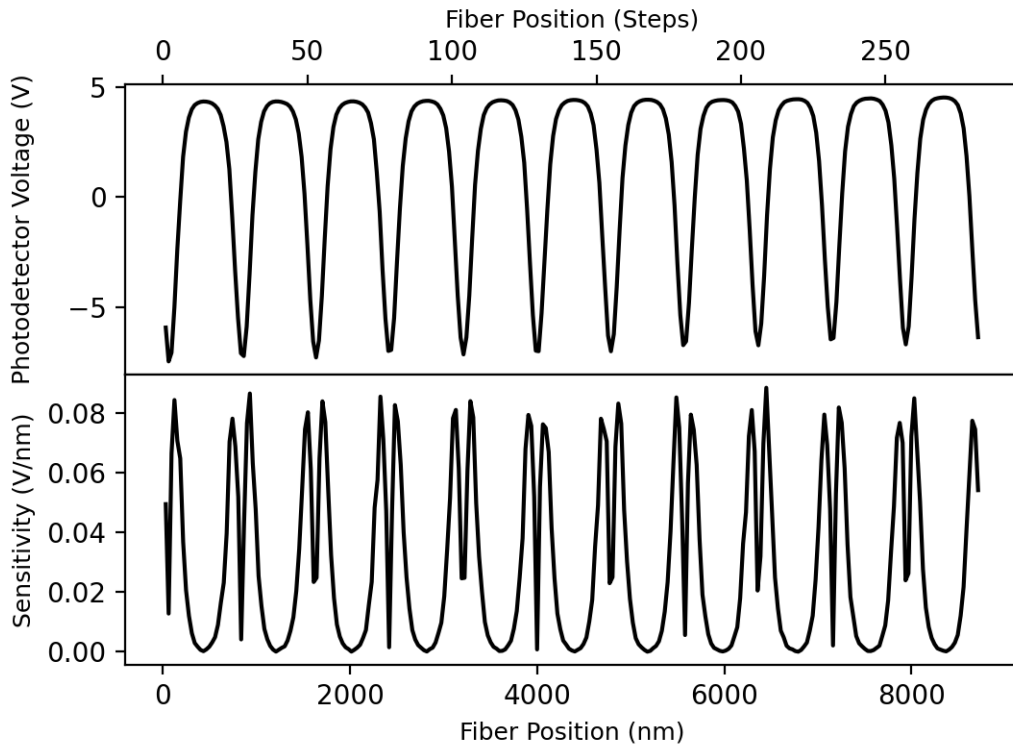


Figure 3.6: Detection laser signal and interferometer sensitivity as a function of fiber position with respect to cantilever (measured in both walker steps and nm). The nm position scale is derived from taking the separation of constructive interference peaks to be half of the laser wavelength ($\lambda/2=775$ nm). Sensitivity is the spatial gradient of the detection signal.

Besides alignment, another important reason for changing the position of the optical fiber is for optimizing the sensitivity and SNR of the detection signal. At close separation, the cantilever fiber system behaves as a fabry-pérot interferometer [33]. It is an optical

cavity, where the detection laser reflects multiple times between the cantilever and fiber end with some fraction of the signal being transmitted back through the fiber each time as the detection signal. A closer separation between the the fiber and cantilever will produce a smaller spot size, capturing and transmitting more of the total signal and increasing the SNR. Additionally, as an interferometer, there will be an alternating pattern of constructive and destructive interference along the signal path. By changing the fiber position, the system will be "walked" through the interference fringes, as shown in Fig 3.6. It is ideal to position the fiber in the middle of an interference fringe, where the spatial gradient of the detection signal is the highest. This way, the oscillation of the cantilever will cause the greatest change in photodetector voltage providing a higher sensitivity.

3.1.2 Electronics

Signal Lock-in Electronics

One of the key elements of effective FM-AFM operation of the LT-AFM is tracking the cantilever response frequency. This is done using a phase-locked loop (PLL) (MFLI, Zurich Instruments). A PLL tracks the oscillation frequency of the cantilever by demodulating it with a phase shifted reference frequency set with a PI controller. By controlling PI gains and the bandwidth of the system, the noise and response time of the frequency signal can be optimized for the given application. This is relevant as when imaging faster response may be required, whereas with spectroscopy lower noise is better. The PLL takes the detection signal as an input, however, it is first amplified and low pass filtered to remove the larger DC component of the photodetector signal.

Scan Control:

To perform the actual function of imaging or spectroscopy using the LT-AFM, the data signals must be read and simultaneously used to inform the motion of the piezo tube scanner by outputting the correct voltages. This is done using an open source scanning probe microscopy controller (Model MK2-A810, SoftdB). Frequency shift and dissipation

signals are read and scanner voltages are output to adjust the position and restore the set-point. Because of the low dynamic range of the controller ($\pm 10\text{V}$) and the high range of the piezo tube ($\sim 300\text{V}$), an intermediate high voltage amplifier is used.

Amplitude Control and Self Oscillation Electronics

A separate signal controller is used to modulate the amplitude, measure the dissipation and run self oscillation of the cantilever (easyPLL plus, Nanosurf). The same amplified, filtered detection signal used for frequency detection is taken as the input signal. A 90° phase shift is applied and it is used to modulate the drive laser signal for self oscillation. Additionally, the controller can be set to provide a variable gain to the output signal so that the cantilever amplitude maintains a fixed set-point. This gain will be read out as the dissipation signal as discussed in section 2.1.4.

Temperature and Pressure Sensing:

As the LT-AFM is operated at vacuum and low temperatures, accurate temperature and pressure sensing is important. The pressure is monitored using a pirani gauge in the $1000 - 10^{-3}$ mbar range and a cold cathode ionization gauge in the $< 10^{-3}$ mbar range. Both are run using a total pressure gauge controller (TPG 300, Pfeiffer Vacuum). Each of the pressure sensors is integrated at the top of the feedthrough tube, further from the vacuum pump than the microscope body. This is to ensure pressure measurements at the sample are never underestimated, as the pump efficiency and therefore vacuum will be higher at the sample. To measure the temperature, a cryogenic temperature probe is integrated on the microscope body as close to the sample as possible to give an accurate reading. The temperature probe is read using a controller (Lakeshore Cryotronics).

3.1.3 Vacuum and Cryogenics

One of the largest determinants of an effective experimental run of the LT-AFM is efficiently pumping and cooling the system. The LT-AFM is not actively cooled and is in-

stead brought to temperature by immersing it in either liquid nitrogen or liquid helium. Poor management of cooling and pumping can result in low vacuum hold time and faster boil-off which cuts experimental time short, or can result in the condensation of ice on the microscope components.

After the microscope can is closed and it is inserted into the dewar, the microscope is pumped down. Using a combined roughing and turbo pump, the microscope pressure can be reduced to the necessary level, $\sim 10^{-4}$ in anywhere from 8-24 hours. The pump time is dependent on a number of factors: how long it has been exposed to atmosphere, cleanliness of the microscope surface after handling and quality of the seals on the many feed-throughs.

Most experiments performed on the LT-AFM are done at liquid helium temperatures (4 K) because of the lower noise and electron thermal energies. However, helium is expensive, typically has long lead times and is a very inefficient coolant with a low latent heat of vaporization. Therefore it is necessary to first cool the microscope from room temperature using liquid nitrogen to a temperature of 77 K. Upon filling the dewar with liquid nitrogen, the microscope body itself would remain close to room temperature as it is effectively vacuum insulated. This is intended, as the inner surface of the microscope can will cool first, causing any moisture to condense on it and not the sample while further reducing the pressure. After allowing a few hours to allow any remaining moisture to condense, the microscope is flooded with helium gas to a pressure of ~ 1 mbar. This is an exchange gas, allowing heat to transfer more effectively from the microscope body into the liquid nitrogen for faster cooling.

After the microscope is cooled, the process is repeated for liquid helium cooling. First, the microscope is pumped down again and the liquid nitrogen is removed from the dewar. Then the liquid helium is transferred into the dewar, this time using a vacuum insulated transfer line due to its lower temperature and higher boil off. A liquid helium transfer requires approximately 40L, 10L to cool the transfer line and dewar and 30L to fill. One helium fill provides approximately 60-72 hours of experiment time before com-

plete helium boil off. Even when cooling to helium temperatures, it is often necessary to characterize the interferometer, cantilever Q factor and perform scans at at both 293 K and 77 K beforehand to ensure the system is working. It is also necessary to separate the sample, cantilever and fiber as they move closer together during cooling.

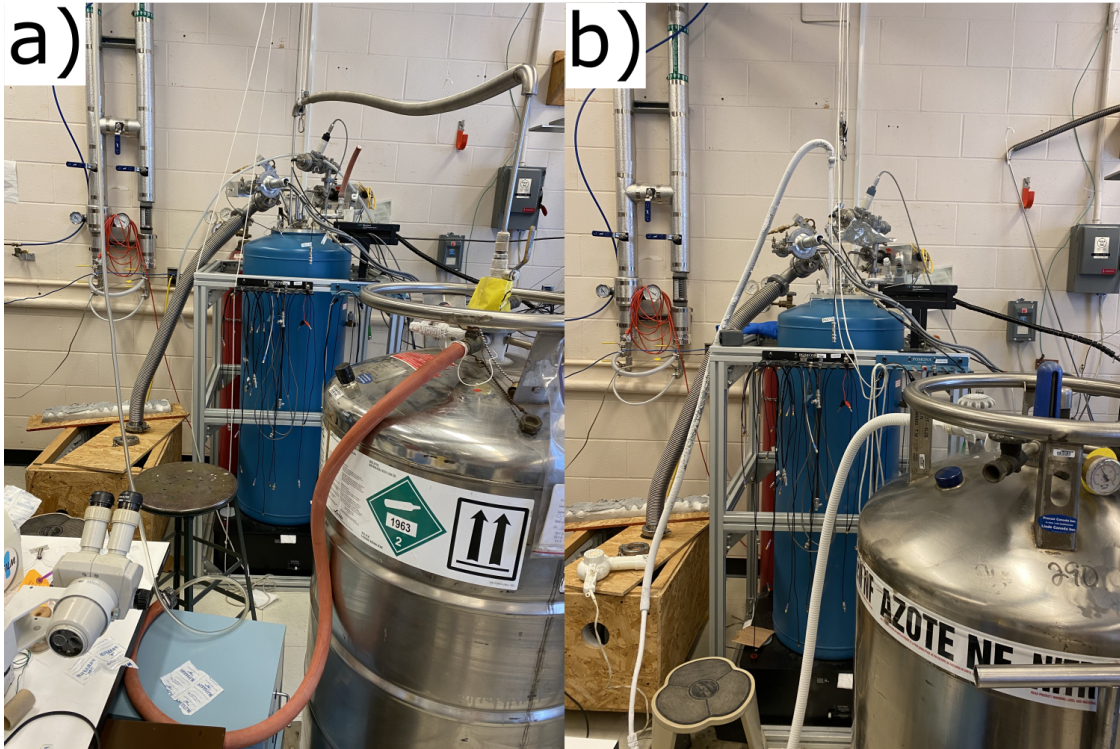


Figure 3.7: (a) Transfer of liquid helium and (b) liquid nitrogen. Because the liquid nitrogen dewar is pressurized, nitrogen will flow out when the valve is opened. The helium dewar is not pressurized, requiring manual pressurization with helium gas for transfer.

To further reduce the vibrational noise of the system, the entire dewar rests on a vibration isolation table (Minus K Technology). The table can be adjusted so that even as the weight of the system changes due to cryogen boil off it will always “float” and be mechanically isolated from the ground. When taking data, the microscope is disconnected from the vacuum system and all electrical cables leading to it are clamped to an external frame. These steps are all taken to reduce all free contact with the outside environment that would add noise to the system.

3.2 Software and Control

GXSM

The Gnome X Scanning Microscopy (GXSM) Project is an open source that allows for multidimensional data analysis and capture and is specifically designed for AFM and SPM [34]. It is able to perform most functionality relating to data capture, reading in up to 8 data channels and controlling sample position and voltage. This allows for automated imaging and spectroscopy. The software additionally has a fully integrated Python console, allowing options for hacked/customizable functionality to be manually added in the future.

LabOne GUI

LabOne is the software suite and associated GUI for interfacing with the signal lock-in electronics, MFLI. The web browser based interface allows for control of the signal lock in settings as well as perform many functions for characterization of the system. Signal outputs defined using LabOne are used in conjunction with GXSM to inform the motion of the scanner. For example, if frequency shift grows too large, a stop signal can be sent to GXSM instructing it to pull the sample as far as possible and protect the cantilever tip from damage.

Script Based Controls

Pressure and temperature reading monitored directly on the LT-AFM control computer. USB connections allow for serial interfacing with both the pressure and temperature sensors, allowing them to be monitored and recorded even when the system is not in use. The detection laser signal is passively read and recorded using a Digilent Analog Discovery 2 (DAD2) PC based oscilloscope. The DAD2 is also used as a controller to generate the saw tooth waveforms required to move the sample and fiber walkers. All customized control and reading through these systems is done using Python scripting.

3.3 Noise and Q Factor Determination

One of the features of the LT-AFM that allows for the measurement of such precise electronic measurements is its incredibly low noise. As the microscope is often disassembled and reassembled to make repairs and replace samples/cantilevers, it is important to validate that it has a similar noise level on subsequent runs. This can be done through analysis of the noise spectral density. The expected amplitude spectral density of the cantilever under thermal/gaussian white noise will be given by [35]

$$N(\omega) = \frac{4k_B T}{\sqrt{k_z Q \omega_0 \{ [1 - (\omega/\omega_0)^2]^2 + (\omega/\omega_0 Q)^2 \}}} + N_{base} \quad (3.1)$$

where N_{base} is the detection noise limit / floor arising from shot and electronic noise intrinsic to the system. By fitting this equation to the frequency domain cantilever detection signal, both the resonance frequency and noise floor can be determined.

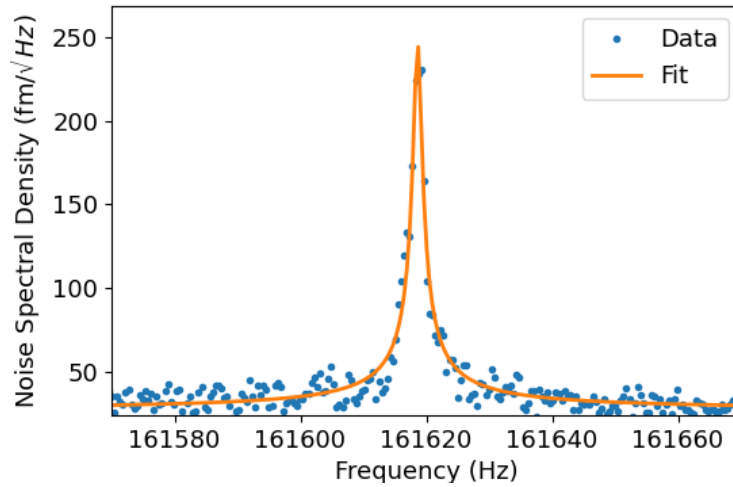


Figure 3.8: Fitted spectral density of the AFM cantilever non-driven resonance peak at 4 K using Equation 3.1. $\Delta f = \Delta\omega/2\pi = 161,619$ Hz, $Q = 113,802$ and $N_{base} = 26$ fm/ $\sqrt{\text{Hz}}$ are calculated from the fit. The data was taken using the FFT mode of MFLI lock-in amplifier and converted from photodetector voltage to femtometers using the calibration process shown in Figure 3.6.

This is shown in Figure 3.8 where the noise floor was calculated as $26 \text{ fm}\sqrt{\text{Hz}}$, consistent with previous measurements [31]. Cantilever Q can also be determined as it is included as a fit parameter. However, Q was calculated as 113,802, inconsistent with the result found using two other methods. The hypothesized reason for this is that Q is associated with the peak width/shape, a feature highly dependent on windowing functions used to obtain the FFT. Additionally, at 4 K, the cantilever Q factor can be so high that a high enough frequency resolution to accurately measure the peak cannot be achieved given the MFLI bandwidth.

Accurate determination of Q is important as higher values result in higher sensitivity measurements and lower values can indicate poor cantilever mounting. Further, Q is necessary to convert excitation gain to dissipation as shown in Equation 2.9. Given that the fitted spectral density method is ineffective at low temperatures, two alternate methods known as ring down and phase slope method were used.

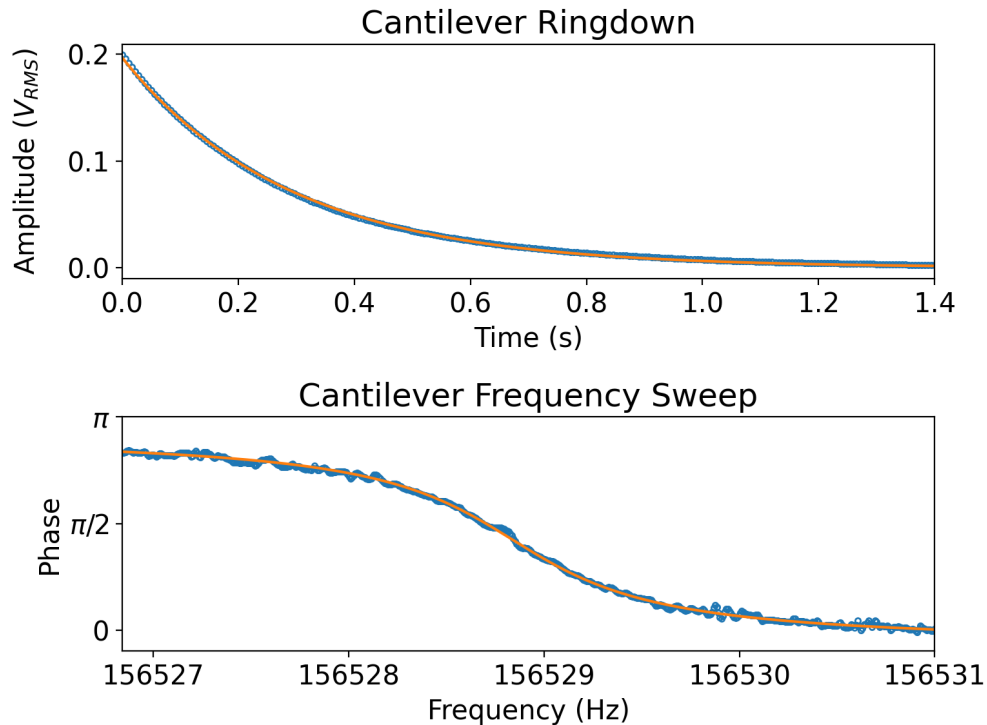


Figure 3.9: Fitted cantilever ring down and phase frequency response at 4 K using eqs. 3.2 and 2.4. The Q factor of the cantilever was found using both methods to be $\sim 140,000$.

The ring down method relies on driving the cantilever to a high amplitude, abruptly removing the driving force, and measuring the decay in cantilever amplitude. The ring down data can be fit using [36]

$$A(t) = A_0 \exp(-\omega_0 t / 2Q) \quad (3.2)$$

The phase slope method requires we perform a frequency sweep of the cantilever near its resonance frequency. As the drive frequency passes through the resonance frequency, the phase offset of the cantilever and the driving force can be expected to follow Equation 2.4. From this fit, the slope of the phase curve at resonance is calculated and used to find Q from [36]

$$Q = \frac{\omega_0}{2} \left| \frac{\partial \phi}{\partial \omega} \right|_{\omega_0} \quad (3.3)$$

Both these methods of determining Q are shown in Figure 3.9. Q found using the ring-down and phase-slope methods were more consistent with each other across multiple experimental runs compared to the spectral density method, and were therefore taken to provide the correct value.

4. Sample Description and AFM Measurements

4.1 SAM and SAQD Samples

The AFM measurements presented in this thesis were made on two different samples. The first is a mixed self assembled monolayer (SAM) of ferrocene terminated and non-functionalized alkanethiols on template stripped gold. This sample was chosen for a number of reasons. Alkanethiols will form a relatively uniform monolayer on a smooth gold substrate. They are non-conducting, acting as a tunneling barrier from the gold electrode, and they are simple to produce, spontaneously forming from solution onto an immersed substrate. Additionally, they can be functionalized with a variety of electrochemically interesting molecules, like ferrocene, or act as a bonding site for other structures, such as gold nanoparticles [37].

Ferrocene is a single redox molecule, meaning it can take either a oxidized (n electrons) or reduced ($n+1$ electrons) state, ideal for single electron charging experiments. Given its structure of two C_5H_5 rings bonded in plane through a single iron atom, it has a well known, low lying vibronic mode characteristic of the two rings rotating with respect to each other [38]. This makes it an effective platform to investigate electron-phonon coupling during single electron charging events and identification of Franck-Condon factors as outlined in Chapter 2.2.3.

Electron-nuclear coupled charging experiments on ferrocene have been previously reported by Antoine Roy-Gobeil [15]. These experiments were performed on SAM incubated from 100% ferrocenylohexadecanethiol ($FcC_{16}SH$). However, this sample preparation procedure can result in a sample surface with too high a density of ferrocene,

making the probing of a single, isolated molecule challenging. Ferrocene molecules are expected to have their charging behaviour altered by the influence of neighboring ferrocene molecules. By incubating substrates in a mixed solution of FcC_{16}SH and non-functionalized pentadecanethiol (C_{15}SH), the density of ferrocene on the sample surface can be controlled. Additionally, the slightly longer thiol chain of FcC_{16}SH allows for confirmation of ferrocene distribution through tapping mode AFM as they will "stick out" above the rest of the monolayer in topography images. Finally, the longer chain length of FcC_{16}SH may allow for observation of even lower vibrational states associated with the oscillation of the thiol itself, not just the ferrocene.

To this end, Harrisonn Griffin outlined a sample preparation and validation protocol as part of his MSc thesis [16]. It involved experimentation with different ratios of FcC_{16}SH to C_{15}SH and both tapping mode AFM and cyclic voltammetry characterization of the samples to ensure appropriate density and distribution of ferrocene. The conclusion of this work was that a molar concentration of 0.05% FcC_{16}SH to 99.95% C_{15}SH produces a sample of some disperse ferrocene molecules and some conglomerated molecules so each can be measured. The same sample preparation protocol was used in this thesis.

To briefly summarize the procedure, first a 500nm layer of 99.99% pure gold is thermally evaporated onto a pristine silicon wafer and allowed to cool. 4x8mm diced chips of a secondary silicon wafer are attached to the gold surface using a thermally activated epoxy and allowed to cure. Using a razor blade, the chips with the now adhered gold layer are pulled off, exposing the clean, wafer side gold surface for incubation. After, the gold substrates are placed in a 1 mM 0.05% FcC_{16}SH to 99.95% C_{15}SH solution in ethanol. The samples are left to incubate for 1 day to 2 weeks and can be used upon removal from the solution.

The other sample measured in this thesis is one consisting of self assembled quantum dots (SAQDs), which are fabricated through a process of *Stranski-Krastanov* growth [39]. This technique relies on the strain induced by lattice mismatch when one semiconductor material is patterned on another material, typically through molecular beam epitaxy [40].

The semiconductor molecules reorganize on the surface, forming nanometer sized blobs that act as QDs. The particular specimen used in experiments consists of, from top to bottom: 1.82 monolayers (ML) of InAs forming the QDs, a 20nm insulating layer of InP, and a 10nm InGaAs layer acting as the back electrode for charging experiments. Additional semiconductor layers exist underneath for the purposes of sample formation but are not involved in the electron transfer process. The resulting QDs formed have the appropriate size and tunneling barrier from the back electrode to show single electron charging at 4K.

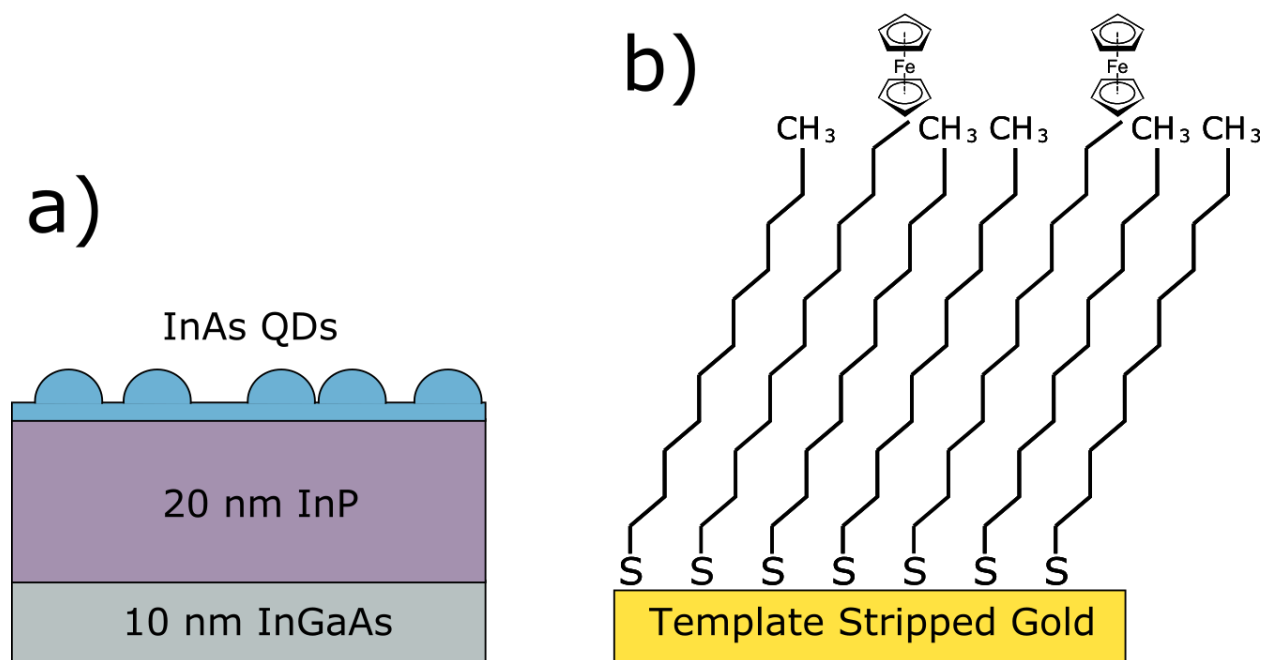


Figure 4.1: Cartoon diagram showing of the general structure of the two samples (a) Self assembled quantum dots and (b) mixed ferrocene capped and non-functionalized alkanethiol self assembled monolayer on gold

4.2 Topography Characterization

Acquiring high quality measurements of charge transfer using AFM is a difficult process. All microscope components need to remain functional after multiple pumping and cooldown steps. Parameters must be finely tuned to elicit and observe charge transfer.

However, one of the most important aspects of the experiments is the sample. As putting a defective sample into the LT-AFM would waste time and resources, it can be extremely valuable to first characterize the sample for evidence of charge traps (QDs or ferrocene capped thiols) using topographical measurements before inserting the microscope into the LT-AFM. This can be performed using a much simpler, AM-AFM system in air. AM-AFM topographical experiments performed for this thesis were done using a Multimode Nanoscope III.

Even after inserting the sample into the LT-AFM, it is useful and common practice to perform topographical measurements. Topographical characterization measurements performed in the LT-AFM are often higher quality resulting from higher sensitivity FM-AFM operation. Finally, topographical measurements are made at both 77 K and 4 K to identify the specific region on a sample with containing charge traps (CTs) for charge transfer measurements.

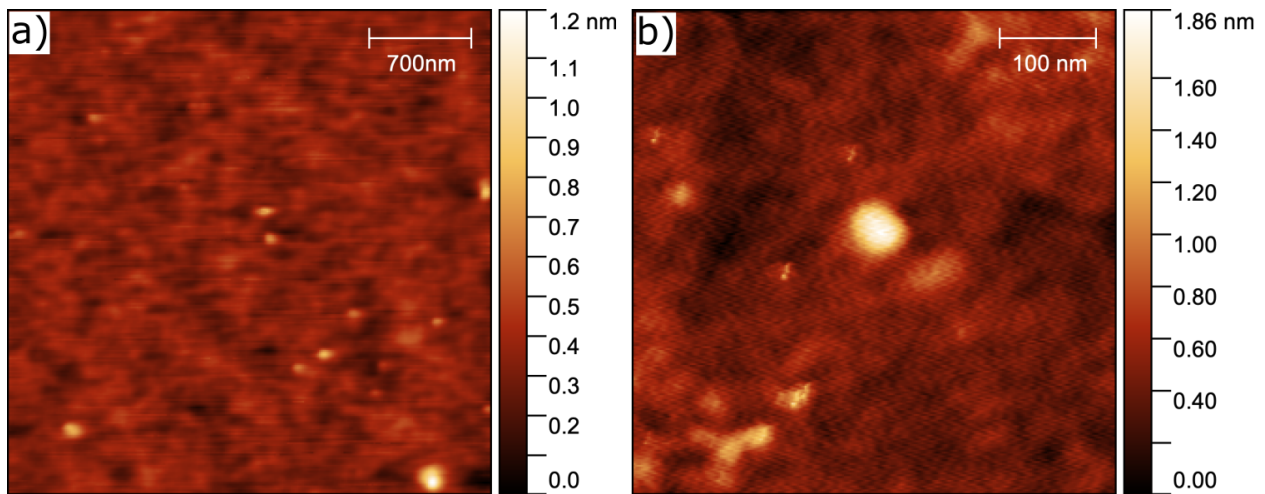


Figure 4.2: Topography images of a SAQD sample. (a) is a FM-AFM $3.3 \times 3.3 \mu\text{m}$ image captured using the LT-AFM at 4 K in non-contact mode. A frequency shift set-point of -15 Hz and a sample bias of -2 V was used. (b) is a FM-AFM 500×500 nm image captured using the LT-AFM at 77 K in non-contact mode. A frequency shift set-point of -20 Hz and a sample bias of 0 V was used. QDs appear as white blobs in the image.

Figure 4.2 shows a SAQD sample imaged with the LT-AFM. Each of the two images is captured with a different scale, sample bias voltage, frequency set point and temperature.

The variation of these features can have the effect of changing the apparent QD topography. A higher sample voltage will cause the tip to feedback off of the longer range electrostatic force, serving to reduce apparent topography and resolution as the tip is further away. A larger frequency set-point magnitude will result in a tip generally closer to the surface that which can provide higher resolution. At lower temperature there is lower thermal noise, also increasing resolution slightly. For this reason, the actual scale of the topography, unless under ideal conditions, is taken as an approximation. Despite this, both Figure 4.2 a and b show a similar height of the quantum dots and consistent distribution given the two image sizes. Though both images are of the same sample, they are not of the exact same region on the sample. Differential contraction of the microscope and the small scan range (4 - 20 μm depending on temperature) makes finding the same image area often impossible after cooling. For this reason, it is important that samples analyzed with the LT-AFM are uniformly coated with structures of interest.

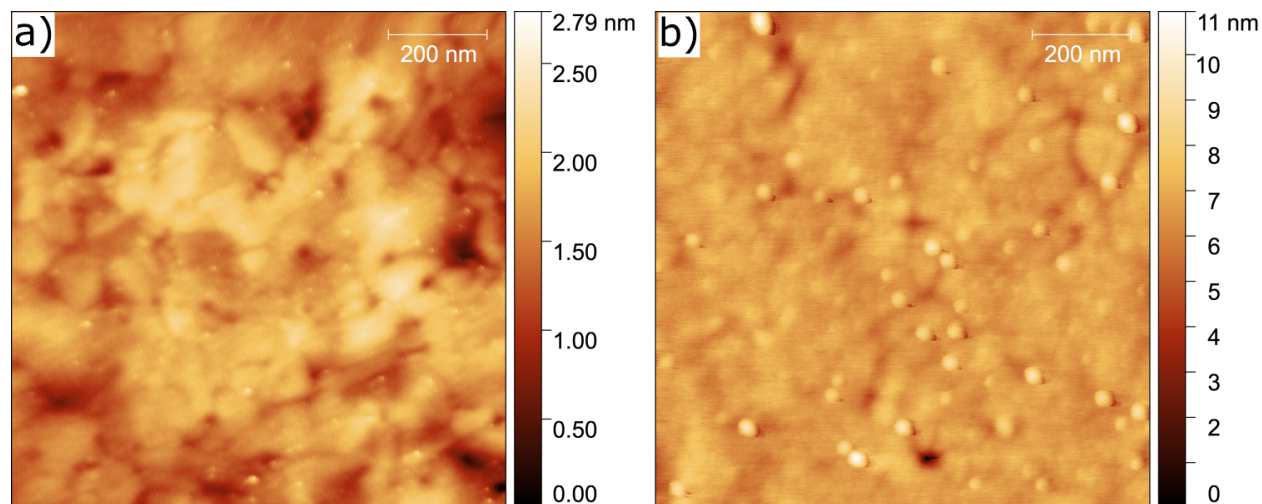


Figure 4.3: Topography images of a ferrocene SAM on gold substrate. (a) is a FM-AFM $1 \times 1 \mu\text{m}$ image captured using the LT-AFM at 77 K in non-contact mode. A frequency shift set-point of -15 Hz and a sample bias of -0.1 V was used. (b) is a AM-AFM $1 \times 1 \mu\text{m}$ image captured using a Multimode Nanoscope III AFM in tapping mode. Ferrocene capped thiols appear as raised bumps both images. Grains of the template stripped gold also be discerned, though not very clearly because of the SAM covering the surface.

Figure 4.3 shows a mixed ferrocene SAM sample imaged with both the LT-AFM and a commercial, in-air AFM system (Multimode Nanoscope III). The LT-AFM operating in non-contact mode, given its higher sensitivity, offers a much higher resolution image than the Nanoscope tapping mode image. There is a dramatic difference between the measured relative height of the ferrocene capped thiols to the uncapped thiols for the LT-AFM compared to the nanoscope (~ 0.2 nm vs ~ 1 nm). Given that the two imaging modes are different, this difference in topography is not entirely surprising. Non-contact imaging and tapping mode result in different distance dependent tip sample forces, which can impact topography measurements. Additionally, there may be error in calibration causing a topography discrepancy between the two systems. The important characteristics are the appearance of and even distribution of raised spots in each image, indicating the presence of ferrocene capped thiols. For both images this is the case.

4.2.1 Time Dependent Changes in Monolayers

Formation of the mixed ferrocene SAM during incubation is a time dependent process. Previous experimental work has shown that properties of the SAM (coverage, structure, etc) are largely set after 12-18h of incubation and that small improvements, like reduction of defects, may result from a longer 7-10 day incubation [6]. However, upon removal from the incubation solution, the SAM will almost immediately be vulnerable. Oxidation of alkanethiol SAMs occurs on the order of hours to days, depending on the exact chemical species [41, 42]. Specifically, atmospheric ozone reacts with the sulfur head group that attaches the thiol to the gold surface, causing it to desorb and clump [43]. This observation of SAM degradation over time is backed up by tapping-mode AFM images taken of the mixed ferrocene SAM at different times post incubation. The most informative examples are shown in Figure 4.4. At 6 days post incubation, raised islands of various sizes can be seen on the sample surface, with the smaller ones (assumed to be ferrocene capped thiols) 1-2 nm in height. 35 days post incubation, the surface structure has completely changed, resulting in larger, more dispersed raised islands on the surface 10-15 nm in height. This is

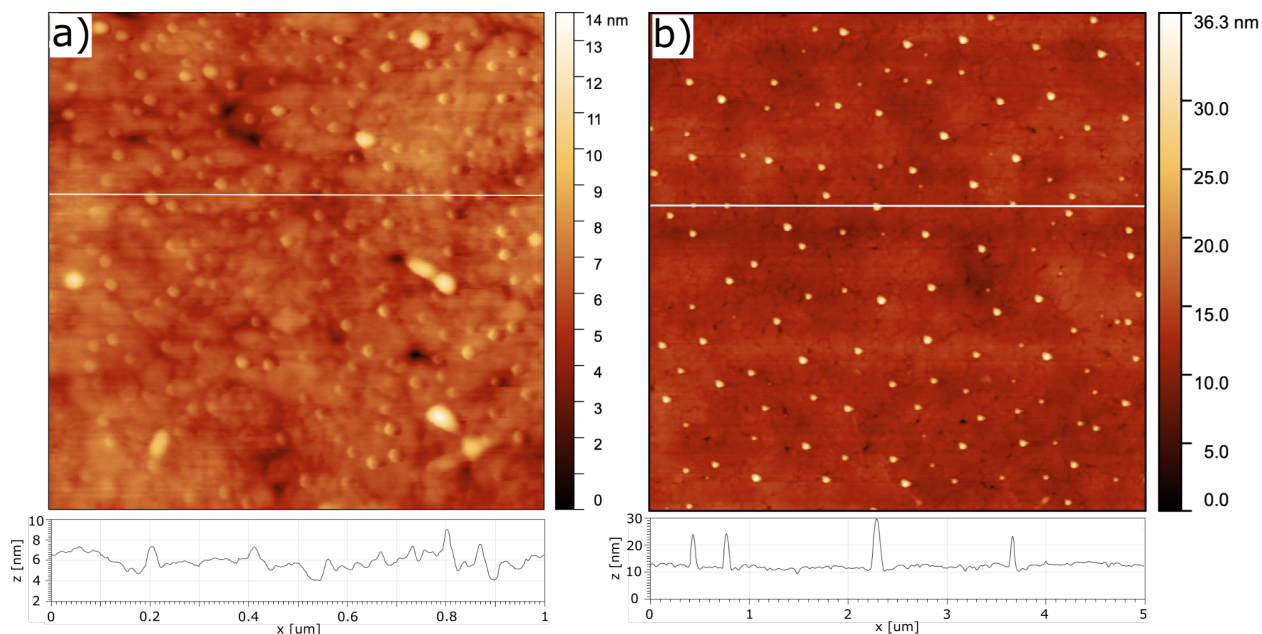


Figure 4.4: Topography images of a ferrocene SAM on gold sample captured using a Multimode Nanoscope III AFM in tapping mode. (a) is a $1 \times 1 \mu\text{m}$ image taken 6 days after removal of the sample from incubation solution and (b) is a $5 \times 5 \mu\text{m}$ image taken 35 days after removal of the sample from incubation solution. A longer sitting time post incubation results in a lower density but greater size of blobs on the sample surface.

taken to be evidence of SAM breakdown and potentially conglomeration resulting from oxidation.

The importance of reducing the SAM in air time post incubation down to < 12 hours was not appreciated until part way through the project. At this point, care was taken to ensure that any SAM sample removed from incubation was placed in the LT-AFM and pumped down on in the same afternoon. A common procedure was to incubate two samples at once with one to be removed first for tapping mode characterization to ensure good formation and the second removed after for LT-AFM characterization.

4.3 Charge Transfer Experiments Through *e*-EFM

As outlined in section 2.1.1, charge transfer can be observed through an increase in frequency shift or dissipation associated with the cantilever oscillation causing an electron

to rapidly tunneling in and out of a CT. This will only occur when the free energy at the CT is tuned to be minimized at the transition from the n to $n+1$ charge state. This tuning can be accomplished by either altering the tip sample bias or the tip sample capacitance via a change in tip position. In charge transfer imaging, the distance between the dot will vary as a function of x and y position of the cantilever. This will produce an image characterized by concentric sets of rings of increased dissipation or frequency shift, corresponding to positions where charge transfer is induced. In bias spectroscopy, peaks in dissipation or frequency shift are observed at tip-sample voltages that for a given tip-dot separation result in induced charge transfer.

As shown in Equation 2.18, the relationship between dissipation and frequency shift will depend on the total tunneling rate. This means in some circumstances evidence of tunneling will be more easily observed in the dissipation channel and other times will be more visible in the frequency shift channel. Additionally, frequency shift images can often be occluded by the electrostatic force background resulting from the raised topography of the charge trap. Frequency shift bias spectroscopy will also have a large quadratic background due to the electrostatic force ($\Delta\omega \propto \Delta V^2$), which must be subtracted off during analysis.

During normal topographic imaging, frequency shift is the feedback signal, allowing the tip and sample separation to remain constant and characterize surface structure. During charge transfer imaging however, the frequency shift is the data signal. We don't want the z position of the tip to change during imaging, therefore, feedback is turned off. Before this is done, the area is first topographically characterized to account for any slope in the sample. This slope is used to inform the z position during scanning and allow for a relatively constant tip sample separation at all points in the image even with feedback turned off.

4.3.1 Self Assembled Quantum Dot Measurements

With the SAQD samples, it is common to find structures that topographically appear as a single QD that are actually multiple dots in close proximity to each other. This is the case in Figure 4.5, with what topographically appeared as two QDs actually being five. Evidence of charge transfer is most visible in the three dissipation images.

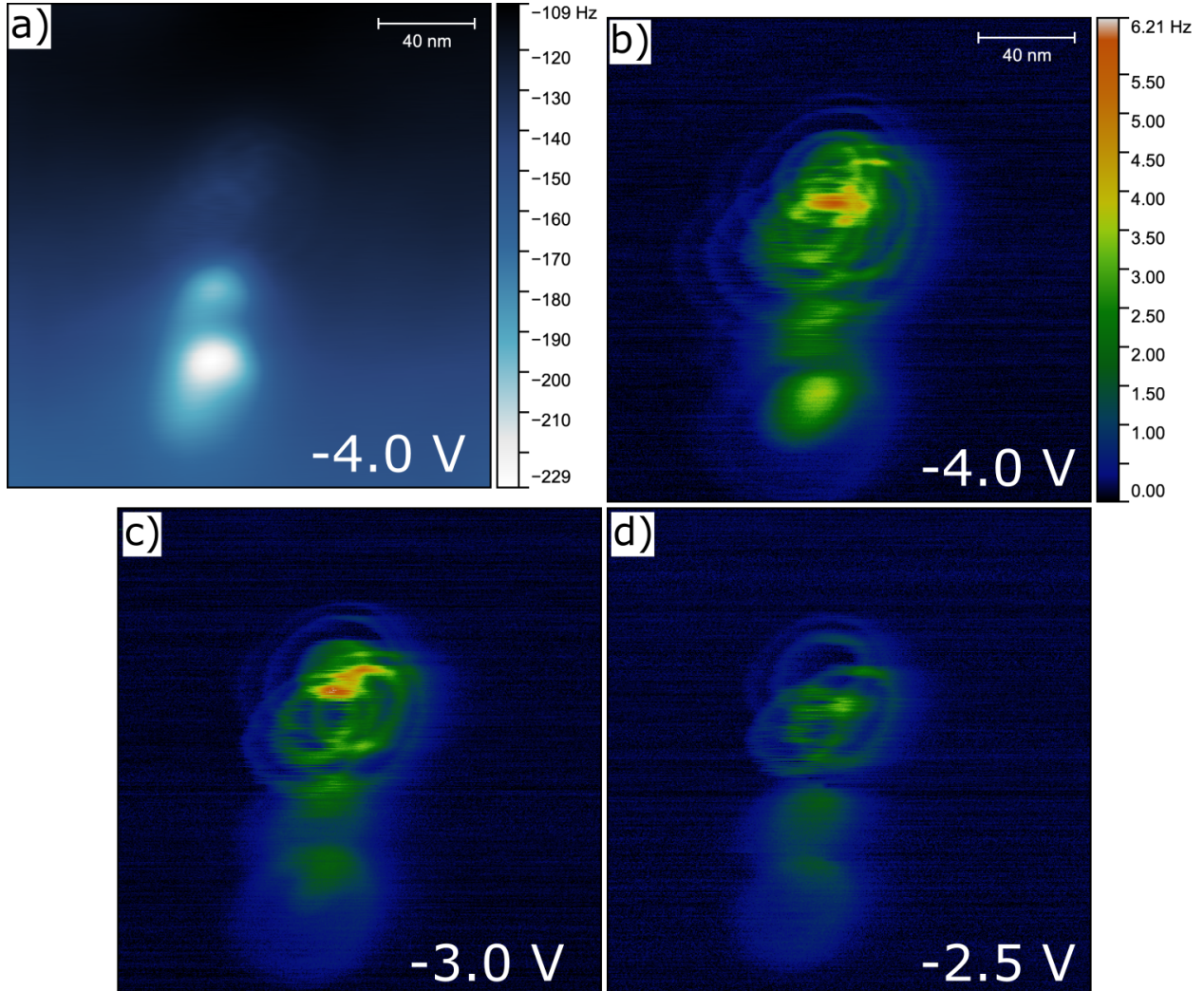


Figure 4.5: Dissipation and frequency shift images of a QD site taken in constant height mode using the LT-AFM at 4 K with different bias voltages. (a) shows the frequency shift channel, while (b), (c) and (d) show dissipation channel. There are 5 observable QDs / CTs, with the topmost 3 being more visible in the dissipation images, while the bottom two are more visible in the frequency shift image.

The outermost ring of a QD will correspond to the first added electron state, with each subsequent ring inward indicating an additional electron addition. The dissipation is also generally stronger for charging rings closer to the center of the dot. As the tip is closer, the change in electrostatic force associated with the change in charge state will be greater, producing a higher dissipation signal.

Regions of the image where rings overlap are positions where the influence of the tip is causing electron tunneling in more than one QD at the same time. The total dissipation signal will be higher as a result of the contribution from multiple QDs. The strongest dissipation signal occurs in the center of Figure 4.5b where crossovers occur between all 3 of the topmost QDs.

It's clear from the differences in the dissipation images that voltage has a large impact on the geometry of the charge transfer regions, given the voltage dependence of tunneling. A higher voltage will allow the first added electron state to be accessed at a lower tip-dot capacitance, meaning the rings will start further away. As a result, there will also be a greater total number of charging rings.

In Figure 4.5a, rings in the frequency shift channel can be vaguely observed in the topmost three QDs. However, the image is largely saturated by the frequency shift signal from the bottom two. Additionally, the bottom two show a weaker dissipation signal with wider rings. These two features suggest that the bottom two QDs are larger in size than the top three. Though sample slope is corrected for in charge transfer imaging, the topography of the QDs themselves are not. As a result, this topography can contribute a large, constant electrostatic force that is recorded as a frequency shift. The frequency shift signal of the bottom two QDs is likely the electrostatic contribution of their topography, with any potential charging ring being too weak to observe. Additionally, it was found in previous experiments that taller dots tend to have a less pronounced dissipation signal [19].

4.3.2 Attempted Ferrocene SAM Measurements

Charge transfer experiments performed on a mixed ferrocene SAM produced unexpected results. As the ferrocene molecule has only two charge states (oxidized and reduced), only one charging ring/peak should be observed. However, as shown in Figure 4.6, structures showing multiple charging events were observed both in images and spectroscopically. Further, the regions where charge transfer was observed had no associated topography signal, meaning the charge trapping structure was below the SAM surface.

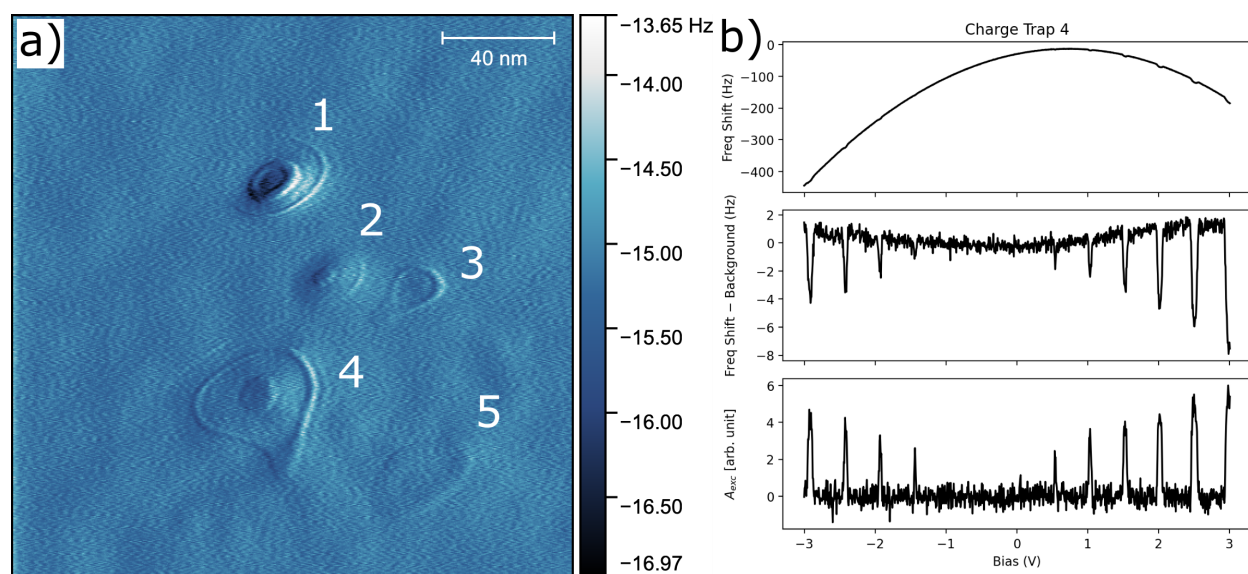


Figure 4.6: (a) Frequency shift images of a SAM sample taken in FM-AFM mode using the LT-AFM at 4 K with a bias of 1V. CTs/ring sites are numbered 1 - 5. (b) shows voltage spectroscopy of CT 4 at a constant height. From top to bottom they are frequency shift, where the tunneling peaks are overshadowed by the electrostatic background; frequency shift with the electrostatic background removed; and the excitation gain for the cantilever drive. This excitation gain is analogous to dissipation (Equation 2.8).

One possibility is that this is a conglomerated mass of multiple ferrocene terminated thiols, showing rings as each molecule is sequentially charged. This would be unexpected, as measurements in section 4.2 showed there to be topography associated with ferrocene thiols. However, some of the ferrocene capped alkanethiols could be adhering to the surface in a non upright orientation, remaining electronically active but providing

no indication through topography. Another possibility is that the SAM formation process resulted in the production of gold nanoparticles from the template stripped gold surface. These particles could then become trapped in the SAM layer, forming gold QDs. This theory is backed up by the variation in the position and spacing of rings associated with the five CTs, which could be arising from gold nanoparticles of different sizes trapped at different depths in the SAM. Despite not being a feature we intended to observe, there are still interesting observations that we can make about these multi-ring CTs.

Though 4.6a is a frequency shift image, it was captured in FM-AFM mode with feedback on (typically used for topography imaging). So, it essentially shows the "error" signal as the frequency shift varies around the set-point of -15 Hz due to charging rings. For this reason, it is challenging to make conclusions from the ring geometry as the tip sample distance is not being held constant. However, it is a useful way to identify the center of a CT so that the tip may be positioned to capture spectroscopic data. Additionally, the non-circularity of the rings at each CT are informative of local variation in the electrostatic sample environment. This likely is not due to a tip shape effect, as the ring deformation is unique at each site.

Figure 4.6b shows an example of the dissipation and spectroscopic data through which charge transfers can be observed. Similar to image data, where charging peaks are observed as a function of tip position resulting in the appearance of rings, charging peaks will appear as a function of voltage in spectroscopy. As the electrostatic force on the tip will also vary as a function of sample voltage and is much larger than the force resulting from single electron charging, peaks will be largely obscured in the raw frequency shift signal. In this analysis, the electrostatic background was modelled and corrected for using a simple quadratic fit, but more detailed correction has been performed by previous students when performing quantitative analysis of frequency peaks [44]. Another interesting feature observed in the raw frequency shift spectrum is how the electrostatic interaction is not minimized at 0 V like one might assume (the parabola is off center). This is the result of a contact potential difference between the tip and sample that primarily

arises as a result of work function difference of the two material, tip geometry, and potential trapped charges in the surface. From the frequency shift spectrum shown in Figure 4.6, the contact potential difference was calculated to be 0.716 ± 0.001 V

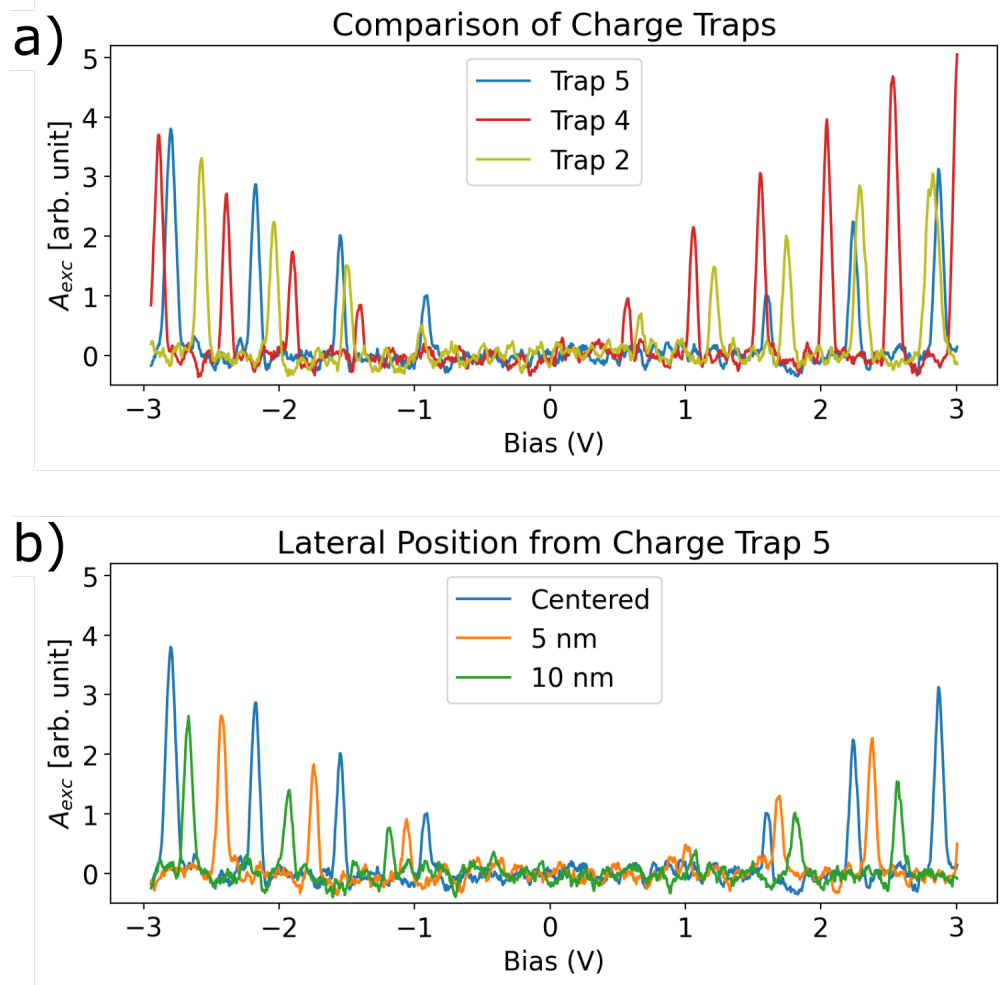


Figure 4.7: Voltage excitation gain spectroscopy of CTs shown in Figure 4.6a. (a) Comparison of spectra captured with the tip centered over 3 different CTs. (b) Comparison of spectra of CT 5 with the tip directly over top, moved 5 nm off center and moved 10 nm off center. In each case, peak height and position is variable

Though observation of charge transfer appears more impressive as images of rings, extraction of tunneling features is typically performed using spectroscopic data. Feature extraction using images would require conversion of tip position to capacitance. This is challenging as determining the exact tip sample z separation requires either touching the

sample or acquiring data at multiple tip sample separations and fitting. Extraction of parameters relevant to tunneling or CT energy levels requires fitting the peak shape. However, the data acquired is not of high enough resolution and the dissipation data could not be accurately calculated for reasons explained in the proceeding section, preventing extraction of quantitative parameters.

To further explore variation in CTs, a variety of spectroscopic measurements were taken, as shown in Figure 4.7. All spectroscopy measurements were taken at the same tip sample separation. Despite this, the excitation gain spectrum varied greatly between CTs 2, 4, and 5 in terms of charge peak height, spacing and voltage corresponding to the first peak. This result is consistent with QDs of different size or different distance from the tip, providing further support the explanation of gold nanoparticles embedded in the SAM layer. Figure 4.7b highlights the importance of accurate positioning when taking spectroscopy measurements. Positioning the cantilever tip just 5 nm off of the center of the dot was enough to produce a substantial difference in peak height, position and spacing. The observed reduction in peak height as the tip is moved away is consistent as the electrostatic force change due to charging is reduced at a further distance.

4.3.3 Excitation Gain Complications and Unintended Self Oscillation

In Figures 4.6 and 4.7, excitation gain measurements were presented instead of dissipation, which was presented in Figure 4.5. The reason for this is the non interacting excitation gain was very small and even negative during the ferrocene data taking run ($A_{exc,0} = -0.05 \pm 0.36$ in Figure 4.6b). This makes calculation of dissipation using Equation 2.9 impossible. One hypothesized reason for this is an unintended self driving effect from the sensing and/or driving laser. The average power of the lasers on the tip will decrease with greater tip fiber separation. As the cantilever oscillates, the power incident on the tip will similarly oscillate. This could provide a driving force on the cantilever, reducing the measured inherent dissipation of the cantilever and even make it self oscillating ($A_{exc,0} < 0$), with no modulation of the drive laser. This proposed effect is supported by

another observation: when advancing or retracting the fiber in the LT-AFM, there were positions where the cantilever would reach very high oscillation amplitude, despite no drive laser modulation amplitude. This means there are regions along the beam path where the cantilever is especially susceptible to this self oscillation. Additionally, this effect was only observed at low temperatures, where the Q factor is higher and the inherent dissipation of the cantilever is already incredibly small.

We believe the fiber was positioned in a region of moderate self excitation during the ferrocene experiments, preventing us from calculating the dissipation. Moving forward, care should be taken to position the fiber so that the intrinsic dissipation/non interacting excitation gain is at a reasonable value and not being self driven. This is a challenging process as detection and drive laser sensitivity are already impacted by fiber position, so a total of three separate conditions must be monitored. Additionally, care should be taken in future experiments to take higher resolution data with longer time averaging so that accurate fitting for extraction of relevant parameters is possible.

5. Conclusions and Outlook

In this thesis, I have presented charge transfer measurements of self assembled quantum dot (SAQD) and mixed ferrocene self assembled monolayer (SAM) samples using single electron electrostatic force microscopy (*e*-EFM). Observation of dissipation and frequency shift peaks in both imaging and spectroscopic data have allowed for a discussion and summary of the main observable features of charge transfer and how quantitative factors may be extracted. Unexpected results of a ferrocene sample showing no topography signal and multiple tunneling peaks warrant further investigation. Time permitting, more experimentation should be performed on mixed ferrocene SAMs to search for charge transfer sites that are both topographically and electronically active, as well as acquire higher quality data more suitable for quantitative analysis. This could allow for validation of these charge transfer sites as either conglomerated ferrocene or gold nanoparticles buried in the SAM.

To confirm previous analysis on the short shelf life of SAMs, I performed AFM topography measurements on ferrocene SAMs at a variety of post incubation times, finding significant structural changes associated with longer exposure to air. Previous experiments have and planned future experiments will utilize SAMs in different forms to study molecules of interest. This work should highlight the importance of monitoring SAM quality and minimizing contact with air. Sample preparation requiring multiple incubation steps should be done in an oxygen/ozone free environment to maximize the chance of producing a high quality sample.

Noise and *Q* factor determination are both important initial steps in acquiring high quality charge transfer measurement data. I have outlined an effective method for quantifying noise in our low temperature atomic force microscope (LT-AFM) and two independent methods of determining *Q* using cantilever ring down and phase slope. Care

should be taken to repeat these measurements on future LT-AFM runs to monitor system performance over time and accurately normalize dissipation data.

Bibliography

- [1] N. Elgrishi, K. J. Rountree, B. D. McCarthy, E. S. Rountree, T. T. Eisenhart, and J. L. Dempsey, "A practical beginner's guide to cyclic voltammetry," *Journal of chemical education*, vol. 95, no. 2, pp. 197–206, 2018.
- [2] T. A. Fulton and G. J. Dolan, "Observation of single-electron charging effects in small tunnel junctions," *Physical review letters*, vol. 59, no. 1, p. 109, 1987.
- [3] Y. Chen, "Nanofabrication by electron beam lithography and its applications: A review," *Microelectronic Engineering*, vol. 135, pp. 57–72, 2015.
- [4] Z. Lu, J. Zheng, J. Shi, B.-F. Zeng, Y. Yang, W. Hong, and Z.-Q. Tian, "Application of micro/nanofabrication techniques to on-chip molecular electronics," *Small Methods*, vol. 5, no. 3, p. 2001034, 2021.
- [5] F. A. Aldaye, A. L. Palmer, and H. F. Sleiman, "Assembling materials with dna as the guide," *Science*, vol. 321, no. 5897, pp. 1795–1799, 2008.
- [6] J. C. Love, L. A. Estroff, J. K. Kriebel, R. G. Nuzzo, and G. M. Whitesides, "Self-assembled monolayers of thiolates on metals as a form of nanotechnology," *Chemical reviews*, vol. 105, no. 4, pp. 1103–1170, 2005.
- [7] S. Anantathanasarn, R. Nötzel, P. Van Veldhoven, F. Van Otten, Y. Barbarin, G. Servanton, T. dE VRIES, E. Smalbrugge, E. Geluk, T. Eijkemans, *et al.*, "Lasing of wavelength-tunable (1.55 μ m region) in as/ in ga as p/ in p (100) quantum dots grown by metal organic vapor-phase epitaxy," *Applied Physics Letters*, vol. 89, no. 7, p. 073115, 2006.
- [8] G. Binnig, C. F. Quate, and C. Gerber, "Atomic force microscope," *Physical review letters*, vol. 56, no. 9, p. 930, 1986.

- [9] C. Schönenberger and S. Alvarado, "Observation of single charge carriers by force microscopy," *Physical Review Letters*, vol. 65, no. 25, p. 3162, 1990.
- [10] M. T. Woodside and P. L. McEuen, "Scanned probe imaging of single-electron charge states in nanotube quantum dots," *Science*, vol. 296, no. 5570, pp. 1098–1101, 2002.
- [11] R. Stomp, Y. Miyahara, S. Schaer, Q. Sun, H. Guo, P. Grutter, S. Studenikin, P. Poole, and A. Sachrajda, "Detection of single-electron charging in an individual inas quantum dot by noncontact atomic-force microscopy," *Physical review letters*, vol. 94, no. 5, p. 056802, 2005.
- [12] L. Cockins, Y. Miyahara, S. D. Bennett, A. A. Clerk, S. Studenikin, P. Poole, A. Sachrajda, and P. Grutter, "Energy levels of few-electron quantum dots imaged and characterized by atomic force microscopy," *Proceedings of the National Academy of Sciences*, vol. 107, no. 21, pp. 9496–9501, 2010.
- [13] L. Cockins, Y. Miyahara, S. D. Bennett, A. A. Clerk, and P. Grutter, "Excited-state spectroscopy on an individual quantum dot using atomic force microscopy," *Nano letters*, vol. 12, no. 2, pp. 709–713, 2012.
- [14] A. Roy-Gobeil, Y. Miyahara, and P. Grutter, "Revealing energy level structure of individual quantum dots by tunneling rate measured by single-electron sensitive electrostatic force spectroscopy," *Nano Letters*, vol. 15, no. 4, pp. 2324–2328, 2015.
- [15] A. Roy-Gobeil, Y. Miyahara, K. H. Bevan, and P. Grutter, "Fully quantized electron transfer observed in a single redox molecule at a metal interface," *Nano Letters*, vol. 19, no. 9, pp. 6104–6108, 2019.
- [16] H. Griffin, "Ferrocene-terminated self-assembled monolayers for the electrochemical non-contact afm detection of single electron redox events," Master's thesis, McGill University, 2020.

- [17] T. R. Albrecht, P. Grütter, D. Horne, and D. Rugar, "Frequency modulation detection using high-q cantilevers for enhanced force microscope sensitivity," *Journal of applied physics*, vol. 69, no. 2, pp. 668–673, 1991.
- [18] S. Morita, R. Wiesendanger, and E. Meyer, eds., *Noncontact Atomic Force Microscopy*. Springer, hardcover ed., 7 2002.
- [19] L. Cockins, *Atomic force microscopy studies on the electrostatic environment and energy levels of self-assembled quantum dots*. PhD thesis, McGill University, 2010.
- [20] R. Waser, *Nanoelectronics and information technology*. Weinheim, Germany: Wiley-VCH Verlag, Mar. 2003.
- [21] Y. Miyahara, A. Roy-Gobeil, and P. Grutter, "Quantum state readout of individual quantum dots by electrostatic force detection," *Nanotechnology*, vol. 28, no. 6, p. 064001, 2017.
- [22] J. Park, A. N. Pasupathy, J. I. Goldsmith, C. Chang, Y. Yaish, J. R. Petta, M. Rinkoski, J. P. Sethna, H. D. Abruña, P. L. McEuen, *et al.*, "Coulomb blockade and the kondo effect in single-atom transistors," *Nature*, vol. 417, no. 6890, pp. 722–725, 2002.
- [23] J. Koch, F. Von Oppen, and A. Andreev, "Theory of the franck-condon blockade regime," *Physical Review B*, vol. 74, no. 20, p. 205438, 2006.
- [24] K. H. Bevan, A. Roy-Gobeil, Y. Miyahara, and P. Grutter, "Relating franck-condon blockade to redox chemistry in the single-particle picture," *The Journal of Chemical Physics*, vol. 149, no. 10, p. 104109, 2018.
- [25] A. Troisi, "How quasi-free holes and electrons are generated in organic photovoltaic interfaces," *Faraday Discussions*, vol. 163, pp. 377–392, 2013.
- [26] A. Tekiel, Y. Miyahara, J. M. Toppole, and P. Grutter, "Room-temperature single-electron charging detected by electrostatic force microscopy," *ACS nano*, vol. 7, no. 5, pp. 4683–4690, 2013.

- [27] S. Rast, C. Wattering, U. Gysin, and E. Meyer, "The noise of cantilevers," *Nanotechnology*, vol. 11, no. 3, p. 169, 2000.
- [28] M. Roseman, *Low Temperature Magnetic Force Microscopy Studies of Superconducting Niobium Films*. PhD thesis, McGill University, 2001.
- [29] "MS Windows NT kernel description." <https://www.nanoandmore.com/AFM-Tip-240AC-PP>. Accessed: 2022-06-18.
- [30] D. M. Weld and A. Kapitulnik, "Feedback control and characterization of a micro-cantilever using optical radiation pressure," *Applied Physics Letters*, vol. 89, no. 16, p. 164102, 2006.
- [31] Y. Miyahara, H. Griffin, A. Roy-Gobeil, R. Belyansky, H. Bergeron, J. Bustamante, and P. Grutter, "Optical excitation of atomic force microscopy cantilever for accurate spectroscopic measurements," *EPJ Techniques and Instrumentation*, vol. 7, no. 1, p. 2, 2020.
- [32] J. Yang, *The mechanics of piezoelectric structures*. Singapore, Singapore: World Scientific Publishing, Dec. 2006.
- [33] B. Hoogenboom, P. Frederix, J. Yang, S. Martin, Y. Pellmont, M. Steinacher, S. Zäch, E. Langenbach, H.-J. Heimbeck, A. Engel, *et al.*, "A fabry-perot interferometer for micrometer-sized cantilevers," *Applied Physics Letters*, vol. 86, no. 7, p. 074101, 2005.
- [34] "Gnone x scanning microscopy." <http://gxsm.sourceforge.net/>. Accessed: 2022-07-06.
- [35] K. Kobayashi, H. Yamada, and K. Matsushige, "Frequency noise in frequency modulation atomic force microscopy," *Review of Scientific Instruments*, vol. 80, no. 4, p. 043708, 2009.

- [36] J. M. L. Miller, A. Ansari, D. B. Heinz, Y. Chen, I. B. Flader, D. D. Shin, L. G. Villanueva, and T. W. Kenny, "Effective quality factor tuning mechanisms in micromechanical resonators," *Applied Physics Reviews*, vol. 5, no. 4, p. 041307, 2018.
- [37] X. Cui, A. Primak, X. Zarate, J. Tomfohr, O. Sankey, A. Moore, T. Moore, D. Gust, G. Harris, and S. Lindsay, "Reproducible measurement of single-molecule conductivity," *science*, vol. 294, no. 5542, pp. 571–574, 2001.
- [38] J. Bodenheimer and W. Low, "A vibrational study of ferrocene and ruthenocene," *Spectrochimica Acta Part A: Molecular Spectroscopy*, vol. 29, no. 9, pp. 1733–1743, 1973.
- [39] I. N. Stranski and L. Krastanow, "Zur theorie der orientierten ausscheidung von ionenkristallen aufeinander," *Monatshefte für Chemie und verwandte Teile anderer Wissenschaften*, vol. 71, no. 1, pp. 351–364, 1937.
- [40] D. Leonard, K. Pond, and P. Petroff, "Critical layer thickness for self-assembled islands on gaas," *Physical Review B*, vol. 50, no. 16, p. 11687, 1994.
- [41] M. H. Schoenfish and J. E. Pemberton, "Air stability of alkanethiol self-assembled monolayers on silver and gold surfaces," *Journal of the American Chemical Society*, vol. 120, no. 18, pp. 4502–4513, 1998.
- [42] T. M. Willey, A. L. Vance, T. Van Buuren, C. Bostedt, L. Terminello, and C. Fadley, "Rapid degradation of alkanethiol-based self-assembled monolayers on gold in ambient laboratory conditions," *Surface Science*, vol. 576, no. 1-3, pp. 188–196, 2005.
- [43] N. Sandhyarani and T. Pradeep, "Oxidation of alkanethiol monolayers on gold cluster surfaces," *Chemical physics letters*, vol. 338, no. 1, pp. 33–36, 2001.
- [44] A. Roy-Gobeil, *Single-electron charging using atomic force microscopy*. PhD thesis, McGill University, 2016.